Controlling The Emission From Semiconductor Nanocrystals Using Optical Microcavities

Yueyue Zhao

May 18, 2013

Abstract

Semiconductor optical microcavities play a vital role in controlling the interaction between light and matter. By coupling a single nanocrystal in the microcavity, its spontaneous emission can be modified. In order to fully exploit the microcavities, it is critical for the nanocrystal to be resonant with the cavity mode spectrally and spatially, respectively. Spectral tuning and spatially matching are very challenging.

However, the work presented in the thesis has overcome these challenges. The realisation of a fully tunable microcavity with a hemispherical feature for semiconductor nanocrystals experiments is demonstrated at room temperature. The cavity wavelength is tuned by changing the separation between the mirrors and spatial tuning is achieved by introducing an $x - y$ positioner.

Photoluminescence data from a single nanocrystal within the cavity is presented at room temperature. The Purcell effect is observed for a single nanocrystal where is spatially positioned at the exact antinode of the electric field.

Acknowledgements

I would like to thank my supervisor Dr. Jason Smith for his invaluable support and insightful discussions during this year.

Thanks are given to every member in the PNG group, in particular Dr. Aurelien Trichet for enormous encouragement, guidance and patience.

Thanks Johnny Fill for his help with preparing nanocrystal solutions and Naomi Omori my fellow Part II student.

Finally I would like to thank eBioscience for supplying nanocrystals.

Contents

1 Introduction **5**

1.1 Motivations and Objectives 5

1.2 Outline 6

2 Operation Principle of Single Photon Source **8**

2.1 Introduction 8

2.1.1 Quantum confinement 8

2.1.2 Auger relaxation mechanism 9

2.2 Optical Microcavity 11

2.2.1 Q-factor, finesse and free spectral range (FSR) 11

2.2.2 Gaussian modes 13

2.2.3 Distributed Bragg Reflectors (DBR) 15

2.3 Purcell effect (weak coupling) 16

2.3.1 Spontaneous emission rate in free space 16

2.3.2 Spontaneous emission rate in single mode cavity 17

3 literature review **19**

3.1 Introduction 19

3.2 Coupling a single QD to a cavity mode 19

3.3 RT operations based on QD-microcavity coupled systems 21

3.4 Open access microcavities 24

4 Engineering applications **27**

5 Optical characterisation **29**

5.1 Introduction 29

5.2 Room temperature transmission setup 29

5.3 Cavity analysis for transmission experiments 31

5.4 Summary 38

6 Nanocrystals in Optical microcavities **39**

6.1 Introduction 39

6.2 Experimental setup 39

6.3 PL spectra from nanocrystals coupled to optical microcavities 41

6.4 Coupling a single nanocrystal to a cavity 46

6.5 Summary 51

7 Time-Resolved Photoluminescence of a single nanocrystal in a microcavity **52**

7.1 Introduction 52

7.2 Modified lifetimes by spectral tuning 52

7.3 Analysis of spontaneous emission rate 54

7.4 Modified lifetimes by spatial tuning 59

7.5 Conclusions 62

8 Conclusions and future work **63**

8.1 Conclusions 63

8.2 Future work 64

9 Project management **65**

9.1 Objective 65

9.2 Initial results 65

9.3 Time management 66

9.4 Unexpected Problems 66

9.5 Innovation 67

Chapter 1

Introduction

1.1 Motivations and Objectives

One of the most exciting challenges in quantum optics is to develop techniques of controlling interactions between single photons and matter. Beyond the scope of the fundamental importance in optic science, single quantum emitters have been explored in playing key elements in a photonic quantum network: storing and processing quantum information. With the development of interconnected quantum networks, more applications are expected to contribute in the fields such as quantum communication and quantum cryptography [1][2]. Possibilities of single photon sources (SPS) include single atoms [3], ions, molecules [4], nitrogen vacancy (NV) centres [5] and semiconductor quantum dots (QDs) [6][7]. However, colloidal nanocrystals (NCs) are the candidates that will only be used in this project. Colloidal nanocrystals represent the most promising materials at room temperature because of their attractive characteristics: compatibility with mature semiconductor technologies [8], narrow spectral linewidth and ease of integration with optical microcavities. In addition, broad tunable emission range and high quantum efficiency render nanocrystals become sufficient for the fabrication of SPS [9][10]. Nevertheless, many studies reported that colloidal nanocrystals suffer from peculiar features of fluorescence intermittency and long luminescence lifetime ($\sim$ 20 ns) [11][12][13], which limit their applications in single-photon emitting devices [14]. Although several approaches have been investigated to conquer these drawbacks, an elegant strategy of embedding single emit-

ters inside quantum-confined microcavities is considered as the most effective way to alter their emission properties and radiative lifetime. In this work, the target is to place a single QD in a tunable cavity at room temperature. A QD randomly emits single photons in any directions; however, the emission will be directed into the cavity mode when it is coupled to a cavity mode. The spontaneous emission (SE) rate into that mode will be enhanced thereby the rate of photon production will be increased. Well-defined spatial and spectral mode structures lead to strong lateral and vertical confinements of the light, which are characterised by low loss (high quality factor) and low volume microcavities.

Our research group has fabricated novel open access microcavities by focused ion beam milling [15], and that the solution-based single nanocrystal coupled to a microcavity and Purcell effects [30] at room temperature have been observed [16]. Nevertheless, such solution-based system suffers from severe problems with reproducing single nanocrystal experiments because a single nanocrystal in solution is hardly to be placed stably in the microcavity. In this thesis, the experiment was also carried out at room temperature with same colloidal nanocrystals. However, the nanocrystal solution was spin cast on the mirror, which gives a lot more control as nanocrystals are fixed in position. Moreover, a new design of experimental setup for single nanocrystal-microcavity has been developed, providing more degrees of freedom for nanocrystals. On the basis of great efforts on developing the single nanocrystal experiments, the cavity coupled single nanocrystal emission and Purcell enhancements have been achieved. In addition, promising results of single mode emission have been highlighted that can be substantially useful for SPS.

1.2 Outline

In this thesis, some relevant properties of QDs, optical microcavities and cavity quantum electrodynamics system will be explained in chapter 2. I will also discuss some of the literature published to date as well as engineering applications (chapter 3 and 4). Chapter 5 is devoted to a discussion of experimental data of empty optical microcavities obtained from transmission experiments. After this, the major interest in this work, results from several photoluminescence (PL) experiments will be presented, with an emphasis on the

observation of Purcell effects on a single QD in a microcavity in time-resolved photoluminescence measurements (chapter 6 and 7). Finally, I will end with a chapter to conclude the achievement of this work, and the discussion of future directions.

Chapter 2

Operation Principle of Single Photon Source

2.1 Introduction

Colloidal semiconductor nanocrystals are composed of an inorganic core with an organic terminated surface (ligands). This outer layer chemically and electrically passivates the nanocrystal surface, while giving the capability of being dispersed in various solutions to prevent agglomeration. The material of primary interest here is cadmium-selenide (CdSe) with a capping layer of zinc-sulphide (ZnS). The ZnS, having a higher bandgap, passivates the surface better than the ligand, and hence it is commonly used as a shell of CdSe to increase the quantum yield. The most important driver of interest in such materials is the change in optical and electrical properties that occurs when nanocrystals alter from bulk behaviour to quantum dots via a quantum mechanical effect, known as quantum confinement [17].

2.1.1 Quantum confinement

Reducing the dimensions of a direct bandgap semiconductor can lead to quantisation of the continuum energy levels. Quantum confinement occurs when excitons in QDs are confined in the order of the electron and hole de Broglie wavelengths. This confinement

results in the changes in electronic density of states (DOS), which is defined as the density of available energy states per unit energy [18]. The electron density of states, $n(E)$, in the bulk semiconductors increase monotonically as the energy is increased, which is shown in equation 2.1,

$$n_{3D}(E) = \frac{1}{2\pi}(\frac{2m_e}{\hbar^2})^{\frac{3}{2}}E^{1/2} \tag{2.1}$$

Equation 2.1 shows the electron can occupy a continuum of energy levels. Therefore limited control over the optical properties is realised in the bulk system, and electrical properties can only be modified through doping effect by introducing extra carriers.

In CdSe/ZnS QDs, the electron is restricted in all three spatial dimensions that no k space is available to fill up with electrons and each quantum state can only be occupied by two electrons. Ideally the DOS of QDs is characterised by a $\delta-$function and atomic-like behaviour of QDs gives rise to the discrete energy level. In practice, however, the DOS of QDs is formed as a set of Lorentzian shapes with a linewidth of $\sim$ 50 meV at room temperature due to rapid dephasing mechanisms [19]. The electron confinement in QDs induces a shift in optical absorption towards a higher energy compared to bulk materials [20]. A schematic diagram of DOS for QDs and bulk semiconductors is illustrated in figure 2.1.1.

2.1.2 Auger relaxation mechanism

An important exciton dynamical process of single nanocrystals is fluorescence intermittency, also known as blinking. The main mechanism of blinking effects is Auger recombination, which is a relaxation process involving an exciton in the environment of at least one other charge carrier. When the recombination of exciton occurs, energy is transferred to another charge carrier rather than being emitted as photon, seen as figure 2.1.2. Depending on the exciton energy, the extra charge carrier is either placed in a trap state or excited high into the band and rapidly relaxes to the ground state in a few picoseconds

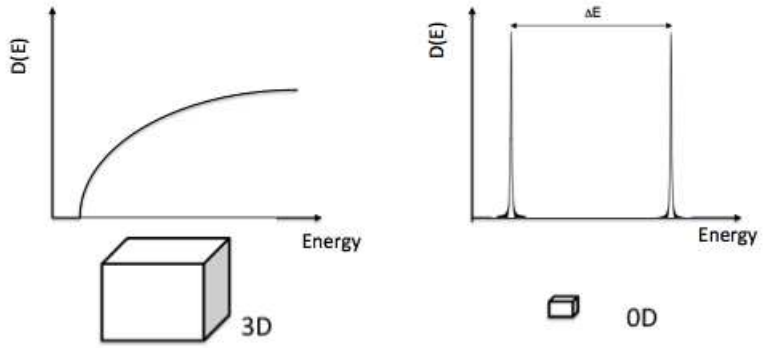

Figure 2.1.1: The electronic density of states for (a) bulk semiconductor and (b) quantum dots. The DOS increases monotonically with energy in bulk system and discrete energy levels are formed in quantum dots with energy separation of ΔE.

(ps) through phonon interactions [21]. Investigations of Auger recombination mechanism in single QDs have shown that the Auger recombination lifetime is directly proportional to the nanocrystal volume, whilst not heavily dependent on material properties. Similar lifetimes have been reported for direct and indirect bandgap materials [22][23][24]. Due to the phenomena of fluorescence intermittency, a single CdSe/ZnS QD exhibits the observation of 'on' and 'off' periods in emission. The 'on' state is described by the radiative recombination of photoluminescence (PL) or photo-excitation, whilst the 'off' state is defined as a non-radiative recombination mechanism. A statistical analysis of intermittency shows a power-law distribution of the bright and dark times.

$$P(\tau) = A\tau^{-\alpha} \tag{2.2}$$

Where A is the fitting parameter and α is the power law exponent.

A strategy to control and prevent blinking has been recently proposed by Mahler and co-workers [25], who showed that a thicker shell in CdSe-CdS nanocrystals allowed one to control the blinking behaviour. The significance of well designed shells are highlighted to obtain non-blinking QDs. Non blinking behaviour has also been observed in ternary CdZnSe/ZnSe nanocrystals, designed as a radial graded alloy of CdZnSe into ZnSe [26].

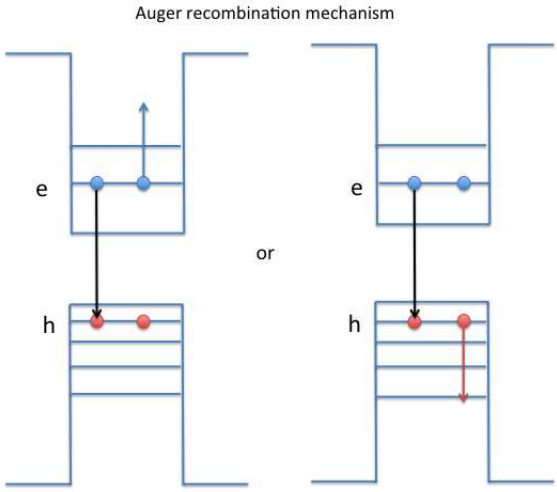

Figure 2.1.2: A schematic of Auger recombination mechanism.

2.2 Optical Microcavity

Optical cavities are a means to confine light on a length scale of photon wavelength to small volumes by resonant recirculation. With the developments in microcavities, optical cavities with dimensions in micro-scale have allowed scientists to observe quantum effects of the light's electromagnetic field. This can no longer be explained by a classical theory of light. The spontaneous emission rate of emitters can be altered by the presence of microcavities. In order to explain the effects of optical microcavities it is useful to gain a thorough understanding of their optical properties.

2.2.1 Q-factor, finesse and free spectral range (FSR)

Q factor is the most common parameter of the cavity, which is a measure of how well the cavity confines photons. The photon lifetime τ_c (the time before a resonant photon scatters out of the cavity) in terms of reflectivity of the mirrors and cavity length is shown in equation 2.3 [27],

$$\tau = \frac{-2L}{c \ln [R_1 R_2 (1-T)^2]} \tag{2.3}$$

Where R_1 and R_2 are the mirror reflectivities, T_i is fractional internal loss per pass

due to diffraction and other internal losses and L is cavity length. The cavity Q factor can be shown as,

$$Q = \frac{2\pi}{\lambda} \frac{-2L}{\ln\left[R_1 R_2 (1-T)^2\right]} = \frac{2\pi c}{\lambda} \tau_c \tag{2.4}$$

Where λ is the resonant wavelength of the cavity.

By a simple Fourier transform, the Q factor can also be measured spectrally as the ratio of a resonant wavelength λ_{res} and the full width at half maximum (FWHM) $\delta\lambda$, given in expression 2.5,

$$Q = \frac{\lambda_{res}}{\delta\lambda} \tag{2.5}$$

An important feature of the Q factor is cavity length dependence, showing that an increase in the Q factor as the cavity length increases. This can be visualised that photons spent more time in flight between collisions in large cavities, allowing each photon stays longer inside the cavity before being scattered out.

Another parameter of cavity is cavity finesse; $\mathcal{F}$ is defined by the ratio of free spectral range (FSR) and the linewidth of a cavity mode or the round trip number of the photon in the cavity (see equation 2.6).

$$\mathcal{F} = \frac{\Delta\lambda}{\delta\lambda} = \frac{\pi\sqrt{R}}{1-R} \tag{2.6}$$

Where FSR (i.e $\Delta\lambda$) is the wavelength separation between successive longitudinal cavity modes, and R is the reflectivity of the mirror. It can be seen from equation 2.6 that high reflectivity of mirrors gives rise to a high finesse, which implies a narrow emission peak. Finesse and Q factor are different figures of merit for capability of light circulation of a microcavity.

Cavity length L can also be written in terms of FSR, provided that the cavity length

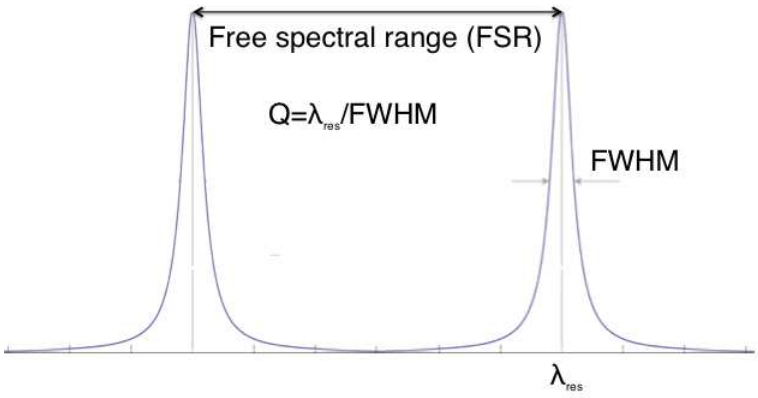

Figure 2.2.1: A schematic of two longitudinal cavity modes, showing defined Q factor and FSR.

is an integer number of half oscillations $L = n\lambda/2$. Rearranging and differentiating this expression the equation 2.7 is shown to be (see figure 2.2.1),

$$\frac{dn}{d\lambda} = -\frac{2L}{\lambda^2} \tag{2.7}$$

Since FSR is the wavelength spacing between adjacent resonances, $dn = 1$ and the equation 2.8 is rewritten as,

$$L = \frac{\lambda^2}{2\Delta\lambda} \tag{2.8}$$

2.2.2 Gaussian modes

The cavity used in this thesis consisted of a planar mirror and a hemispherical mirror that formed cavity modes. The geometry of the half symmetric cavity forms a specific set of Hermite-Gaussian modes, which are solutions of Maxwell's equations [28]. Since these two mirrors have different radii of curvature, a few conditions have to be satisfied to find stable cavity modes. Here resonator g parameters for each mirror is defined as

$$g_i = 1 - \frac{L}{R_i} \tag{2.9}$$

where L is the cavity length, and R_i is the radius of curvature ($i = 1, 2$).

The condition for cavity stability states that $0 \leq g_1 g_2 \leq 1$. In the case of one mirror being planar has $g_1 = 1$ as $R_1 = \infty$. The stability condition reduces to $0 \leq g_2 \leq 1$, which is equivalent to $L \leq g_2$ where R_2 is the radius of curvature of the hemispherical mirror. Since these modes have to be confined into 3-dimensions inside the cavity, a set of integers should be labeled for each mode. One is the longitudinal mode number q, which characterises the confinement along the resonator axis. The higher order transverse mode numbers are designated as m and n, characterising the distribution of electric field in plane perpendicular to the cavity axis and labeling as TEM_{mn} where TEM stands for Transverse Electric Magnetic Field. The frequencies of the Hermite-Gaussian modes depend on q, m and n according to equation 2.10.

$$v_{qmn} = \frac{c}{2L}[q + \frac{1 + m + n}{\pi} \cos^{-1}(g_1 g_2)^{1/2}] \tag{2.10}$$

This shows that different cavity modes are in resonance with different cavity lengths if a single frequency laser is applied. For the longitudinal mode number q (i.e, $m = n = 0$), it is spaced by $c/2L$ and can be calculated as given in expression 2.11.

$$q = \frac{2L}{\lambda} - \frac{1}{\pi} \cos^{-1} \sqrt{1 - \frac{L}{R}} \tag{2.11}$$

The higher order transverse modes with $m+n \neq 0$ are degenerated, which means they have different spatial distributions but the same frequency. The spacing of transverse modes depends on radius of curvature of mirrors so that the spacing between transverse

modes becomes wider as the mirror curvature increases. The radius of curvature related to the spacing of transverse modes and the cavity length is given by,

$$R = \frac{L}{\sin^2\left(\frac{2\pi L \Delta\lambda}{\lambda^2}\right)} \tag{2.12}$$

Where L is cavity length, $\Delta\lambda$ is the spacing of two subsequent transverse modes and λ is the resonant wavelength.

2.2.3 Distributed Bragg Reflectors (DBR)

The distributed Bragg reflectors with pairs of alternating high and low refractive index materials are used to form cavity mirrors, resulting in much higher reflectivity ($R \geqslant 0.99$) than their metallic counterparts ($R \leq 0.98$). Such structures require two contrasting dielectric materials that have an effect of interference to reflect light. When the thicknesses of these layers have 1/4 of wavelength for which the mirror is designed, all reflected components from layer interfaces interference constructively that leads to a very strong reflection in a certain spectral region. The reflectivity of cavities is determined by the number of pairs and by the refractive index contrast between two layer materials. In this thesis silica (SiO_2) and titania (TiO_2) were used due to large difference in refractive indices, where $n_{SiO_2} = 1.46$ and $n_{TiO_2} = 2.25$ respectively. The design of the DBR and of the microcavity was performed through simulations based on the transfer matrix method. Equation 2.13 describes a DBR reflectivity as a function of refractive indices of the materials used and the total number N of dielectric pairs in the structure.

$$R = \left(\frac{1 - \frac{n_s}{n_0}\left(\frac{n_1}{n_2}\right)^{2N}}{1 + \frac{n_s}{n_0}\left(\frac{n_1}{n_2}\right)^{2N}} \right)^2 \tag{2.13}$$

Where n_s and n_0 are the refractive indices of the external media, n_1 and n_2 are refractive indices of the dielectric materials of SiO_2 and TiO_2, respectively. For the case of such DBR mirrors, the field profile shown in figure 2.2.2 is obtained.

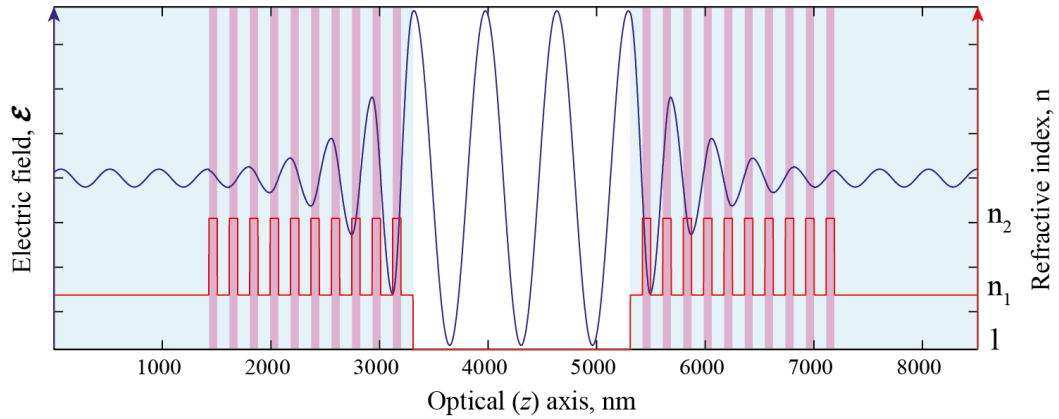

Figure 2.2.2: Field distribution for a cavity length of 2 μm centred at 650 nm. Each cavity mirror contains 10 pairs of silica ($n_1 = 2.1$) and titantia ($n_2 = 2.25$). (Acknowledging P. Dolan for MATLAB code)

2.3 Purcell effect (weak coupling)

The interactions over light and matter were observed when an electric dipole moment was coupled to an electric field distribution in a microcavity, so called cavity quantum electrodynamics (cQED) [29]. In the cQED, there are three key parameters: the decay rate of the cavity (κ), the spontaneous emission decay rate of the atomic system in free space (γ) and the coupling strength between the cavity and the atomic system (g). Depending on the relative magnitudes of these parameters, cQED system can be divided into two physical regimes: weak coupling regime and strong coupling regime. This thesis is only interested in weak coupling regime, which means the spontaneous emission is the dominate mechanism as $\kappa \gg g, \gamma$. An enhancement of the spontaneous emission rate of an emitter in a microcavity is known as Purcell effect [30]. The effect is due to the fact the spontaneous emission rate of an emitter is partly determined by its optical environment, known as density of states (DOS).

2.3.1 Spontaneous emission rate in free space

The spontaneous emission rate of an emitter in free space in given by Fermi's golden rule [31],

$$SE_{free} = \frac{2\pi}{\hbar} \mid \langle p \cdot \varepsilon \rangle \mid^2 \rho(\omega) \tag{2.14}$$

Where $|\langle p \cdot \varepsilon \rangle|^2$ is the probability that there will be transition, p is the dipole moment operator, ε is the electric dipole operator and $\rho(\omega)$ is the photon density of state. The photon density of states in free space is shown as [31],

$$\rho(\omega)_{free} = \frac{\omega^2 V_0}{\pi^2 c^3} \tag{2.15}$$

Where ω is the emitter frequency, V_0 is the cavity volume of an emissive atom.

The electric dipole interaction $|\langle p \cdot \varepsilon \rangle|^2$ can be described as [31],

$$|\langle p \cdot \varepsilon \rangle|^2 = \frac{\mu_{12}^2 \hbar \omega}{6\varepsilon_0 V_0} \tag{2.16}$$

Where μ_{12} is the dipole matrix element. Hence SE in free space can be rewritten by substituting equation (2.14),

$$SE_{free} = \frac{1}{\tau_{rad}} = \frac{\mu_{12}^2 \omega^3}{3\varepsilon_0 \pi \hbar c^3} \tag{2.17}$$

Where τ_{rad} is the radiative lifetime of the emitter. It can be seen from equation 2.17 that the emission rate is proportional to the cube of the frequency of the emitter.

2.3.2 Spontaneous emission rate in single mode cavity

The SE rate from a single emitter coupled to a cavity mode is altered from its free space value due to the modification of the photon DOS by the presence of the cavity.

The photon DOS in a single mode cavity is characterised by a Lorentzian distribution, which is shown as [31],

$$\rho(\omega) = \frac{2}{\pi \Delta\omega} \frac{\Delta\omega^2}{4(\omega - \omega_c)^2 + \Delta\omega_c^2} \tag{2.18}$$

Where ω_c is angular frequency of the cavity mode with a linewidth of $\Delta\omega_c$. On substituting equation 2.18 and equation 2.16 into Fermi golden rule, given that $Q = \omega_c/\Delta\omega_c$. The SE rate of emitter in the cavity can be given by,

$$SE_{cavity} = \frac{2\mu_{12}^2}{\hbar\varepsilon_0}\frac{Q}{V_{mode}}\frac{\Delta\omega^2}{4(\omega-\omega_c)^2+\Delta\omega_c^2} \tag{2.19}$$

The Purcell factor, F_p is defined as the ratio of SE in the cavity and SE in free space.

$$F_p = \frac{SE_{cavity}}{SE_{free}} = \frac{3Q}{4\pi^2 V_{mode}}\left(\frac{\lambda}{n}\right)^3\frac{\Delta\omega^2}{4(\omega-\omega_c)^2+\Delta\omega_c^2} \tag{2.20}$$

Where V_{mode} is mode volume of emitter in the cavity and n is the refractive index of the cavity. At exact resonance where $\omega = \omega_c$, the final expression of F_p is shown as,

$$F_p = \frac{3Q}{4\pi^2 V_{mode}}\left(\frac{\lambda}{n}\right)^3 \tag{2.21}$$

Equation 2.21 demonstrates high Q and low volume cavities are required to maximise the Purcell factor. However this prediction can only be true for the weak coupling regime when linewidth of emitter is smaller than linewidth of cavity. At room temperature, spectral linewidth of the nanocrystals is much broader than the linewidth of the cavity, which is a distinctive characteristic of the bad emitter regime. Therefore emitter Q factor dominates the total effective Q factor but not the cavity's. The expression of Q factor for the combined quantum dot-cavity coupled system is given as,

$$Q_{total} = \frac{\lambda_{peak}}{\Delta\lambda_{cavity}+\Delta\lambda_{QD}} \tag{2.22}$$

Where $\Delta\lambda_{cavity}$ and $\Delta\lambda_{QD}$ are the homogeneous linewidths of the cavity mode and the quantum dot emission respectively [32][33]. At room temperature calculated values of $\Delta\lambda_{cavity} \simeq 0.15$ nm and $\Delta\lambda_{QD} \simeq 14$ nm reduce the effective Q factor from ∼1000 to 45. Therefore the Purcell factor can be determined as a function of $1/V$, provided that small effective Q factor contributed in the Purcell factor.

Chapter 3

literature review

3.1 Introduction

In this chapter, some recent developments of cQED experiments in semiconductor microcavities using QDs are reviewed. Thanks to the appealing characteristics of this project, this chapter will be categorised into three sections: coupling a single QD to a cavity mode, room temperature (RT) operations based on QDs-microcavity coupled systems and open access microcavities.

3.2 Coupling a single QD to a cavity mode

The cavity coupled single nanocrystal is particularly interesting not only from the sights of investigating the cQED effects but also due to the constitutions of the core of SPS [34][35]. The demonstration at low temperature of single photon emission from a single QD with a cavity has been reported since 2001 [36].

In a pioneer work, coupling a single QD to a whispering gallery mode (WGM) of photonic cavities has been presented [37]. In this study, a single CdSe/ZnS QD was bounded to the surface of a single glass microsphere, demonstrating a Purcell effect of 10. Kiraz *et al.* [38] coupled a single self-assembled InAs QD to a microdisk whispering gallery mode using temperature tuning. A crossing behaviour of the WGM and the QD exciton transition is illustrated in figure 3.2.1, which corresponds to the weak coupling

regime. It is noticed that the different temperature dependences of the electronic and optical states lead to the ability to tune QD and the WGM through resonance, and that the temperature dependence of the energy of the WGM is due to the change in refractive index of GaAs with temperature. A sixfold reduction of exciton lifetime and a Purcell factor of 17 were demonstrated in the resonant QD-WGM system. Since the performance of such whispering gallery microcavities are strongly dependent on the quality of interface, optical loss due to scattering and absorption can occur which will be detrimental to the Q factors [39].

Another method of coupling an isolated InAs QD to a cavity mode was also observed in pillar microcavities [40]. In this approach the micropillars were processed using electron beam lithography and reactive ion etching techniques. A single QD array was positioned in a GaAs/AlAs micropillar with a nine-period (top) and a 15-period (bottom) DBR mirrors and a threefold Purcell enhancement was recorded. By using different etching process, Solomon *et al.* used an InGaAs QDs layer with a low density (75 QD/μm^2) in micropillars (Figure 3.2.2(a)), showing a strong modification of the SE rate of a single QD with different spectral detunings with respect to fundamental cavity mode [41]. As shown in Figure 3.2.2(b) where the experimental and theoretical SE lifetime of the resonant QD was plotted as a function of emission wavelength. Compared to the fundamental cavity mode, a smaller Purcell effect was observed for spectrally detuned QDs with emission wavelengths at 895 nm and 897 nm.

A crucial step of deterministically coupled system has been realised by the integration of single site-controlled quantum dots (SCQD) into micropillar cavities [42][43]. High alignment precision was achieved with spatially and spectrally coupled cavity-SCQD system. However, very limited quantum efficiency and oscillator strengths are still suffered from this technique [44]. In order to overcome such drawbacks, far-field optical lithography was developed to achieve deterministic spectral and spatial matching QD microcavities with strong Purcell effect [45]. Recently electrically driven QD-microcavity systems are also developed [46]. The occurrence of photon antibunching at room temperature from single CdSe/ZnS nanocrystals embedded in a vertical microcavity was the first time to be

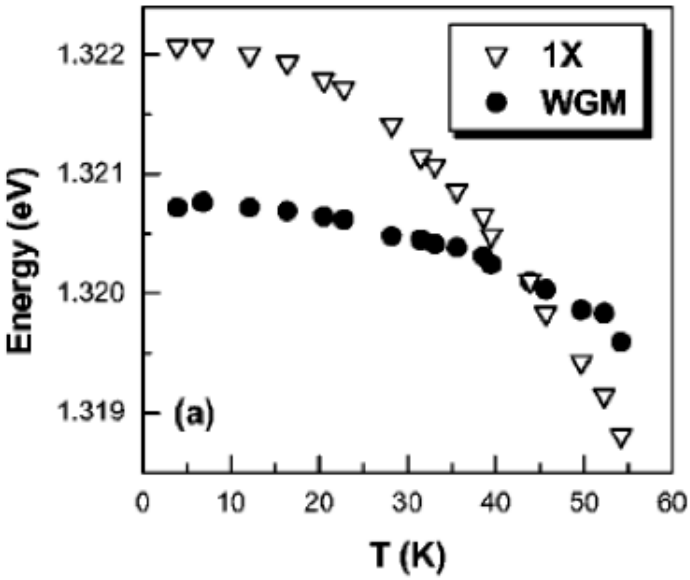

Figure 3.2.1: Change of the WGM and the 1X-transition emission energy as a function of temperature [38]. The temperature dependence of the energy of the WGM gives rise to the change in the refractive index of GaAs with temperature.

demonstrated by Qualtieri *et al.* [14].

3.3 RT operations based on QD-microcavity coupled systems

Although great efforts have been made towards epitaxially grown QDs, the operating temperature of such epitaxial QD-based SPS is still far from room temperature. Nevertheless, recent work has demonstrated Purcell enhancement of the emission from colloidal QDs in the bad emitter regime [16][47].

The demonstration of coupling colloidal QDs to a pillar microcavity mode at room temperature was first established by Qultieri *et al* [14]. Using high-resolution lithographic techniques, CdSe/ ZnS QDs were positioned at the anti-nodes of the standing wave resonant mode between a 4-period top DBR and 4 (bottom) SiO_2/TiO_2 DBR mirrors (see figure 3.3.1(a) and (b)). Figure 3.3.1(c) shows that the radiative lifetime of QDs in resonance with the cavity mode was reduced from 23 ns in bulk to 9.1 ns, resulting in a 2.4x enhancement of the SE rate from QDs. Similarly, same group developed a micropillar consisting of CdSe/ZnS QDs sandwiched between a top SiO_2/TiO_2 $\lambda/2$ DBR of 8 stacks,

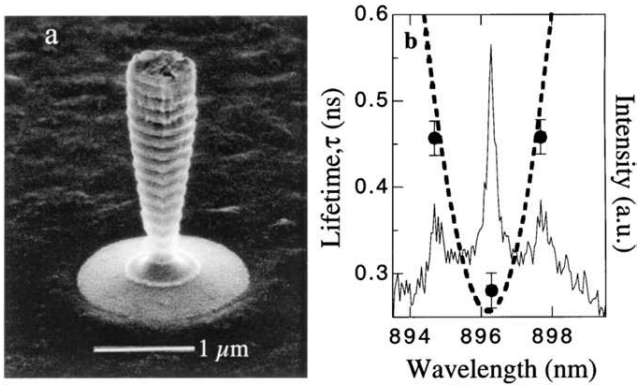

Figure 3.2.2: An SEM image of the device structure (b) A PL spectrum (solid) and the spectral dependence of the spontaneous emission lifetime (filled circles: experimental, dashed line: theory) at 4K. A 4.3x enhancement of the SE rate was shown for a QD in resonant with the fundamental mode than in free- space [41].

and a bottom one with 8 [48]. This arrangement showed the same enhancement of the spontaneous emission lifetime for the localised QDs, which demonstrated the modification of the radiative lifetime is independent on periods of DBR. A decreased Q factor of 2140 was measured that may be caused by the scattering and absorption of the nanoclusters. Recent work on embedding an epitaxially grown quantum dot into MgS barriers up to 300K has been established by Fedorych *et al.* [49], who also proposed that a design of integrating such QDs into micropillars would improve limited outcoupling efficiencies.

Another approach of embedding In(Ga)AS QDs in the photonic crystal microcavities (PCM) has also been studied. Due to the appealing characteristics of small mode volumes and high Q factors, large SE rate enhancements are expected in the PCM. The PCM in figure 3.3.2 was produced by Chen *et al.* [50] and consists of a self-assembled InAs QDs layer embedded at the centre of a GaAs waveguide layer with QD density of 3×10^{10} cm^{-2}. A threefold Purcell enhancement with a Q factor of 150 and volume mode (V_{mode}) of $(\lambda/n)^3$ was recorded, highlighting the importance of using small V_{mode} rather than higher Q to observe SE rate enhancement. Wu *et al.* recorded a Purcell factor of 35 and Q factor of 775 when colloidal PbSe QDs were resonant with a cavity mode of AlGaAs/GaAs PCM, showing the realisation of ultralow threshold lasers for future high-speed circuits [51]. Nevertheless, lower Q factor was measured than predicted one due to heating effects, which would deteriorate the figures of merit.

A further application in RT operations, based on QD-microcavity coupled system,

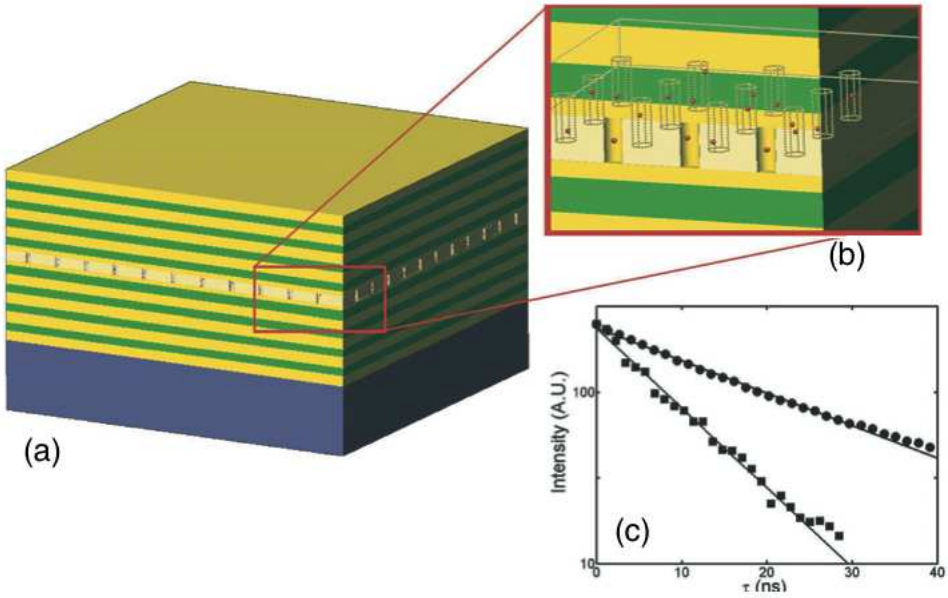

Figure 3.3.1: (a-b) schematics of the whole structure and of cavity region. (c) Lifetime of CdSe/ZnS QDs in/off resonance with a cavity mode. Reproduced from [14]

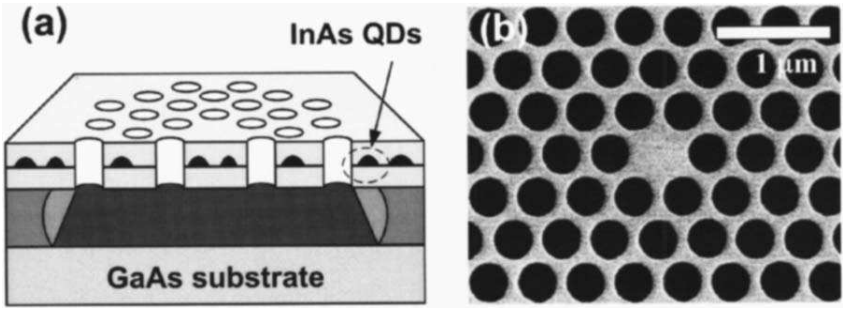

Figure 3.3.2: (a) A schematic of the PC slab structure (one lattice defect was introduced which behaves as a cavity, and the surrounding photonic crystal represents mirrors surrounding the cavity). (b) A SEM micrograph of the PCM with a scale bar of 1μm [50].

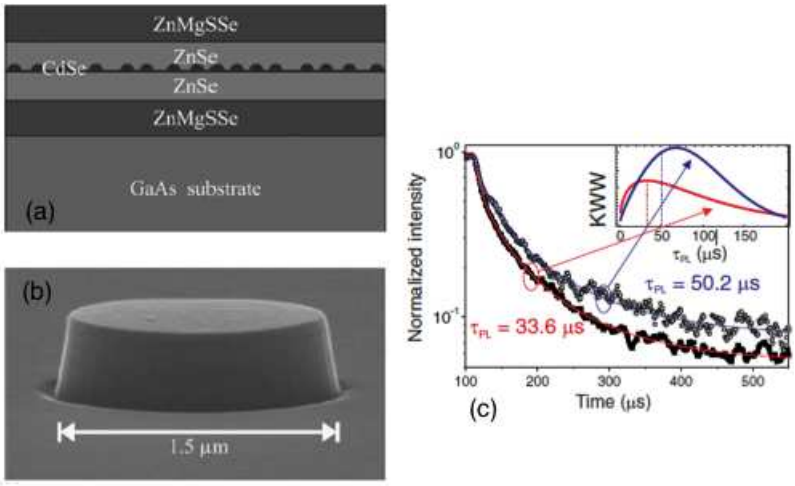

Figure 3.3.3: (a) A schematic of cross section of the epitaxially grown microdisk. Self-assembled CdSe QDs are sandwiched between ZnSe and ZnMgSSe. (b) Side view of a microdisk [52]. (c) PL spectrum of measured out-of-resonance (full squares) and on-resonance (empty circles) [53].

is demonstrated when QDs are embedded in microdisks. The microdisks were fabricated using electron beam lithography and reactive ion etching and mounted on a glass plate [52]. Figure 3.3.3(a) and (b) illustrate the self-assembled CdSe QDs are sandwiched between ZnSe and ZnMgSSe with a diameter of 1.5 μm of the microdisk. This method allows a Q factor exceeding 2000 to be achieved when CdSe QDs are coupled to a whispering gallery mode. Instead of using III-V QDs, SE rate enhancement of Si-nanocrystals has been reported by Pitanti *et al.* [53]. Figure 3.3.3(c) indicates lifetime reductions of 70% have been observed for Si-nanocrystals in resonance with a cavity mode compared to uncoupled ones, which leads to a small Purcell enhancement in the bad emitter regime. However, strong Purcell enhancement could be achieved by fabricating cavities with ultra-small mode volume although Q factors were limited.

3.4 Open access microcavities

As discussed above, integrated approaches using micropillars [36], photonic crystal microcavities [54], and whispering gallery devices [55][56] have been demonstrated. However, unavoidable issues have been suffered from restrictions on *in situ* spectral tunability and spatial tunability. This both limits the science and poses a technological obstacle.

An alternative approach of fabricating microcavities is devoted to an open access

microcavity that contains two opposing mirrors on separate substrates. They have the advantages of being fully wavelength tunable by controlling the cavity length, and cavity mode coupled to optical fibre for efficient collection efficiency of light. A 5x Purcell enhancement has been reported using a planar Fabry-Perot cavity [57]. However, such 1D confinement provides limited control compared with full 3D confinement, and that one way to achieve 3D confinement is to make one of the mirrors concave.

The pioneering experiment on fabricating such spherical micromirrors by latex sphere templating was reported by Prakash *et al.* [58]. In this investigation, V_{mode} can be reduced to 5 μm^3 with Q factors >300 and semiconductor QDs can be deposited on the top mirror, providing an opening door to cQED experiments. Cui *et al.* produced this type of microcavities by forming bubbles in molten silica [59]. With this approach, cavity length of 40 μm and finesses of 200 were achieved for cavities with radius of curvature=50 μm. This work first demonstrated that DBR mirrors were used to embed a QD in a tunable microcavity. Another method involving direct fibre coupling was developed [60]. In this case of microcavities, Muller *et al.* used a DBR coated optical fibre and QD-containing planar substrate, achieving a high Q-factor of 3×10^6 and a lower radius of curvature$\simeq 34\,\mu$m.

More recently, a novel technique of CO_2 laser ablation has been demonstrated to construct a concave feature in a silica substrate [61][62][63][64]. This approach allows the radius of curvature as small as 20 μm and Q factors as large as 10^6. The features of smoothness were also realised with reflective coatings up to 99.997%. Using this technique, spatial and spectral tunings of the Purcell effect on a single InGaAs QD were observed by independently moving flat mirrors in $x - y$ plane and in the z direction (see figure 3.4.1) [63]. The radiative lifetime is shortened from 1.2 ns to 0.38 ns when a QD is in resonance with a cavity mode with respect to off-resonant ones, and that the greatest effect of SE rate enhancement at zero detuning is also demonstrated at low temperature shown in figure 3.4.2.

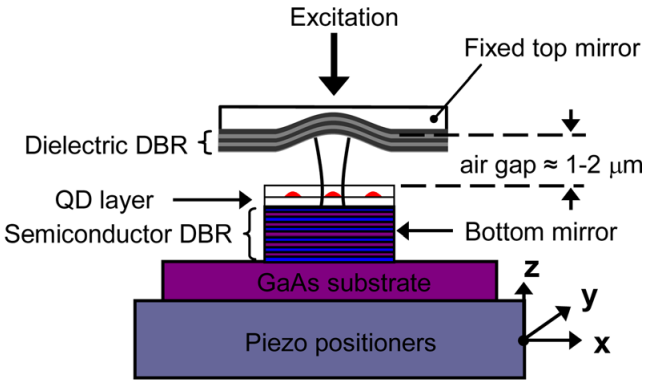

Figure 3.4.1: Schematic of a tunable microcavity for a QD experiment. The hemispherical mirror is fixed in position, while the planar mirror at bottom can be moved in all three dimensions [63].

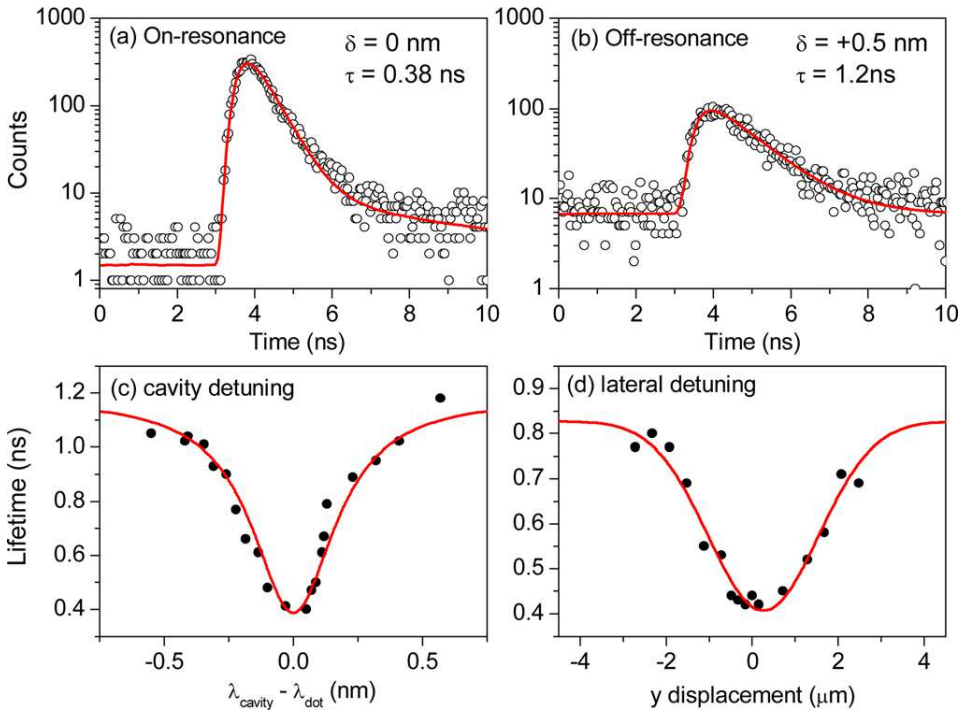

Figure 3.4.2: Lifetime measurement from a single QD in a tunable microcavity. (a) Decay curve at the spatial and spectral resonance. (b) Decay curve of spatial resonance but spectrally detuned by 0.5 nm emission wavelength. (c) (d) lifetimes as a function of detuning spectrally and spatially, respectively [63].

Chapter 4

Engineering applications

The project being undertaken has relevance to applications in single photon sources (SPS). An ideal SPS should only emit a single photon in a pulse, whilst typical coherent light sources (such as a laser) display a Poisson distribution in the number of emitted photons in a time interval. The SPS would be capable of making optical measurements below shot noise level, which is the major limitation in coherent light sources [65][66]. In addition, such a source has the potential of enabling applications in the field of quantum information technology such as quantum cryptography. In the case of quantum cryptography, a SPS emits an array of pulses with each containing only one photon. According to the unavailable modification of the state of a single quantum system, no eavesdropping can occur on a secure communication without being noticed, since the pulse would collapse upon observation by the eavesdropper [67]. Moreover, the SPS can be used to generate indistinguishable photons that can be implemented in quantum computation using linear optical element and single photon detector; this quantum computing can solve problems faster compared to classical computers [67].

All these new applications have allowed the realisation of a practical SPS with three key elements: a single quantum emitter, regulation of the excitation and the recombination process and an efficient output coupling of the single photons [68]. The QD-microcavity system studied in the project is well suited to the requirements of a SPS. The enhancement of SE would possess a shorter radiative recombination time compared to uncoupled single photons, resulting in faster operating speeds. Furthermore, a QD coupled to a cavity can

help the requirement of a SPS to be met since the enhanced light collection efficiencies with higher output coupling of the single photons can be achieved.

Chapter 5

Optical characterisation

5.1 Introduction

In this chapter the optical characterisation of the optical cavities will be discussed. This characterisation of empty microcavities (no coupling to emitters) is carried out by white light transmission.

5.2 Room temperature transmission setup

The transmission setup for microcavities operating at room temperature is illustrated in figure 5.2.1.

A multimode fibre coupled to a white light source was shining through microcavities as shown in figure 5.2.1. The microcavities were formed with a peak reflectivity designed to be at emission wavelength of 640 nm. Each dielectric mirror was formed of 10 periods of $\lambda/4$ $SiO_2(n = 1.4)$ $/TiO_2\,(n = 2.25)$ with a reflectivity of 0.9998, terminated with $\lambda/4$ SiO_2 layer. The final layer allows an anti-node of standing wave mode to be positioned on the mirror surface, where the maximum electric field intensity can be achieved. The 20x magnification objective lens was used with a numerical aperture of 0.4. The transmission spectral information was recorded by a spectrometer with a charged-coupled device (CCD). Since two mirrors have to be parallel to collect as much light as possible, some considerations involved in mounting cavities with efficient degrees of freedom while

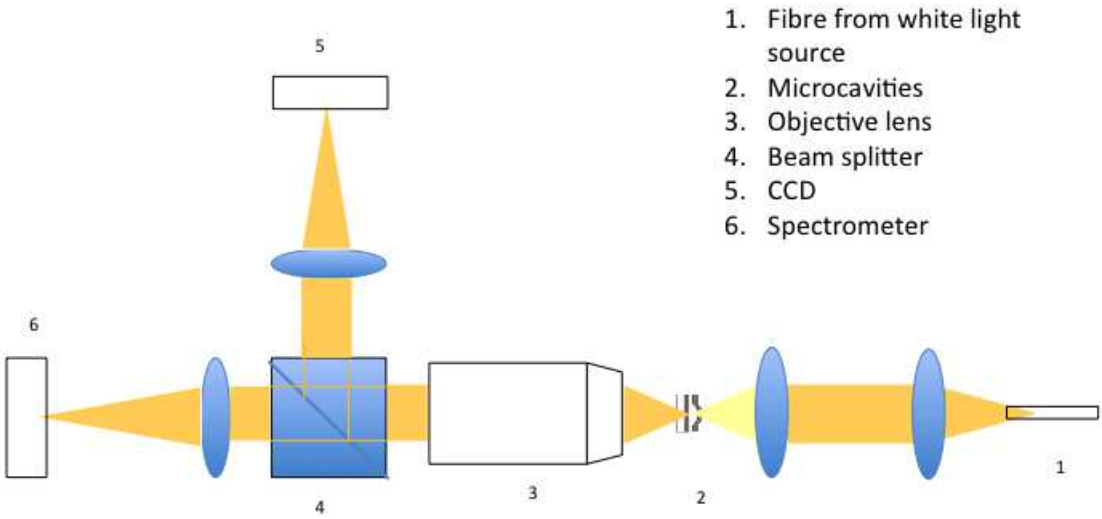

Figure 5.2.1: A schematic of transmission setup.

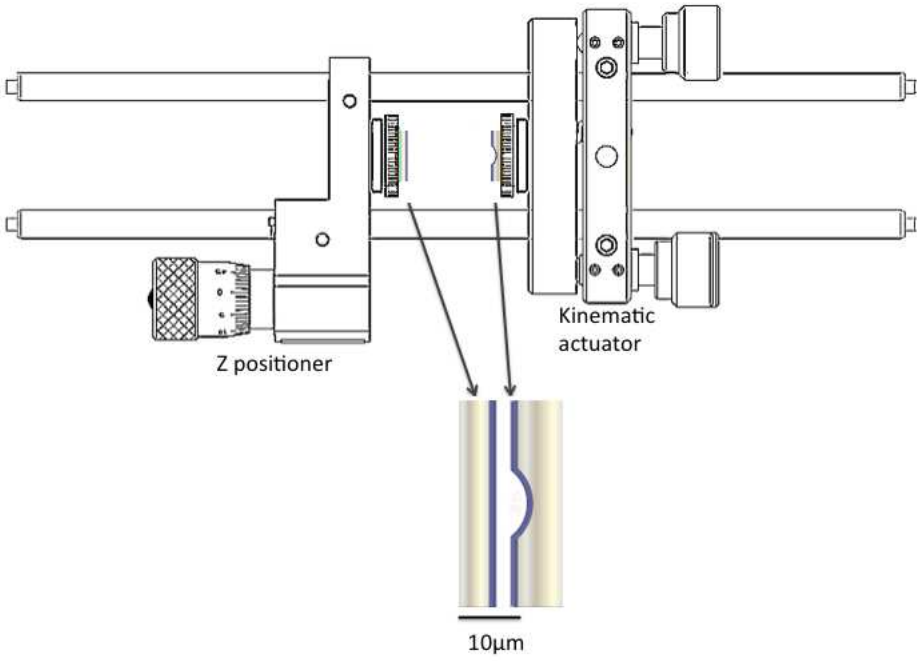

Figure 5.3.1: A schematic of mirrors and manual actuators on a cage rod system. (Acknowledging P. Dolan)

keeping mechanical stability were required.

5.3 Cavity analysis for transmission experiments

As shown in Figure 5.3.1, the planar mirror was mounted on a manual z positioner and the featured mirror was set up on a kinematic actuator, both of which were placed on a cage rod system. By tweaking the screws on the kinematic actuator, the angles of planar mirror were adjusted and the cavity length was controlled by z positioner. The cage system was then mounted to an $x-y-z$ manual positioner, allowing the array of cavities to be tuned in three dimensions relative to illuminated area. When the separation between mirrors is small, linear fringes are seen since two mirrors are tilted with respect to each other (figure 5.3.2). During alignment procedure fringes disappeared if the mirrors were aligned to be parallel with special care. This is significantly vital to obtain the shortest cavity length as well as improve collection efficiency of light.

Figure 5.3.3 illustrates two longitudinal cavity modes only; this can be achieved by precisely illuminating white light spot at the centre of cavity. The cavity length can also

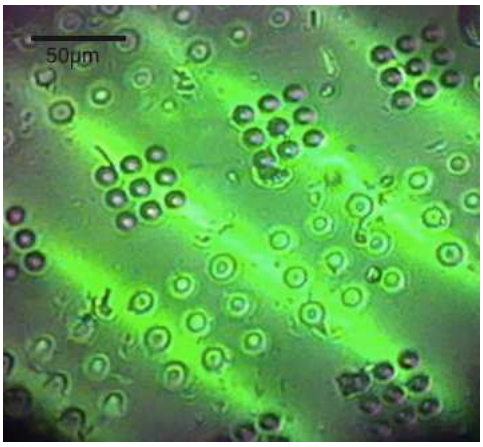

Figure 5.3.2: Interference fringes on the array of microcavities due to misalignment between two mirrors. A scale bar of 50 μm is labeled.

be determined by the free spectral range (FSR), as given in equation 5.1, where n is the reflective index in the cavity.

$$L = \frac{\lambda^2_{resonant}}{2nFSR} \tag{5.1}$$

Since no extra medium other than air was placed between the cavities (i.e n=1), equation 5.1 is simplified as,

$$L = \frac{\lambda^2_{resonant}}{2FSR} \tag{5.2}$$

With the FSR of 76 nm, the cavity length of 2.44 μm is calculated from equation 5.2, provided that the resonant wavelength is centred at 609 nm.

If the cavities were slightly shifted, the white light was illuminated towards the edge of the cavities. This results in several transverse modes to be observed in figure 5.3.4.

Transmission spectra corresponding to a sequential range of cavity lengths were also carried out, as shown in figure 5.3.5. It can be seen from equation 5.2 that the cavity gets smaller as the FSR becomes larger. The shortest cavity length of 2.28 μm was obtained when the longitudinal mode was tuned from 700 nm to 642 nm as the longest FSR was obtained. More importantly, the presence of sequential transverse modes (in figure 5.3.5) provides more useful information for characterising the figures of merit of the cavity that will be discussed in subsequent sections.

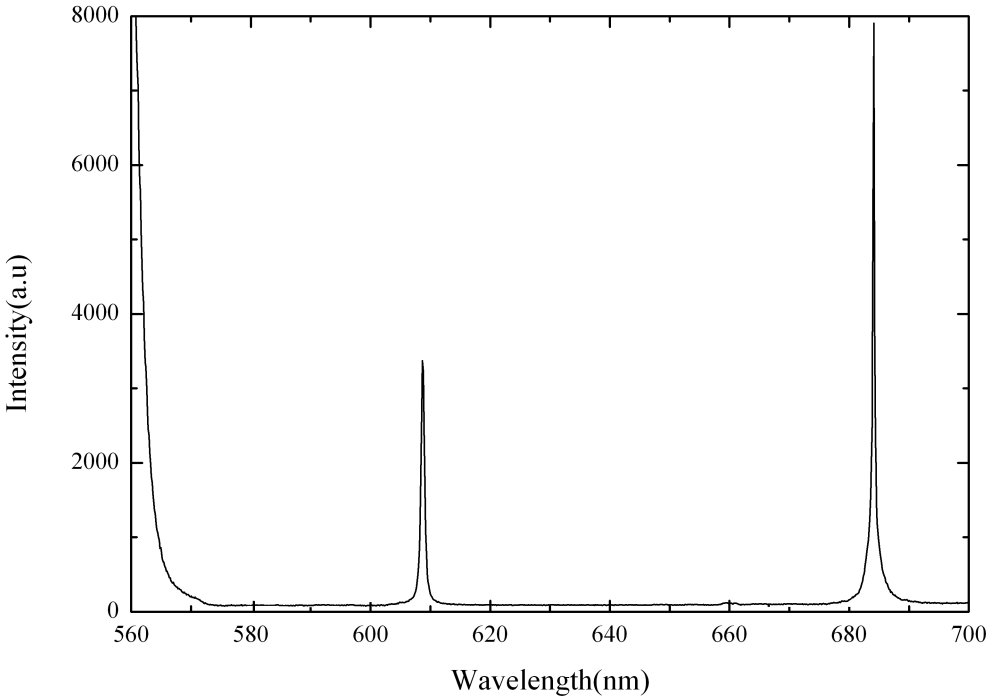

Figure 5.3.3: Transmission spectrum from a small cavity of 2.44 μm with RoC of 25 μm.

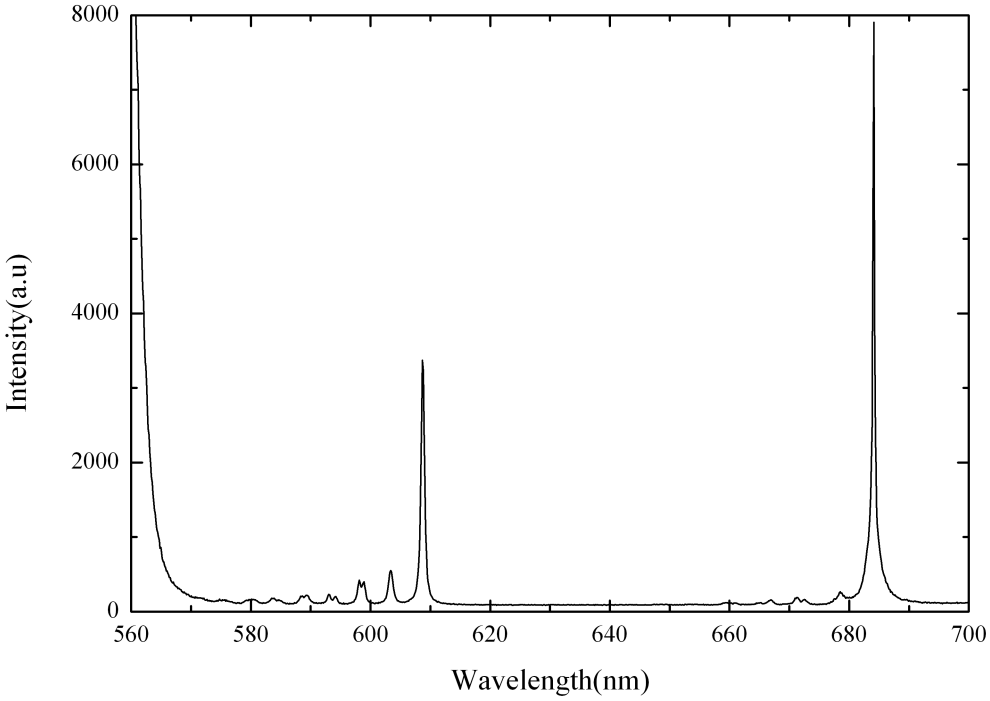

Figure 5.3.4: Spectrum obtained for a cavity with same cavity length compared to that of figure 5.3.3, however light was slightly misaligned with respect to cavities, which allowed higher lateral transverse modes to be excited.

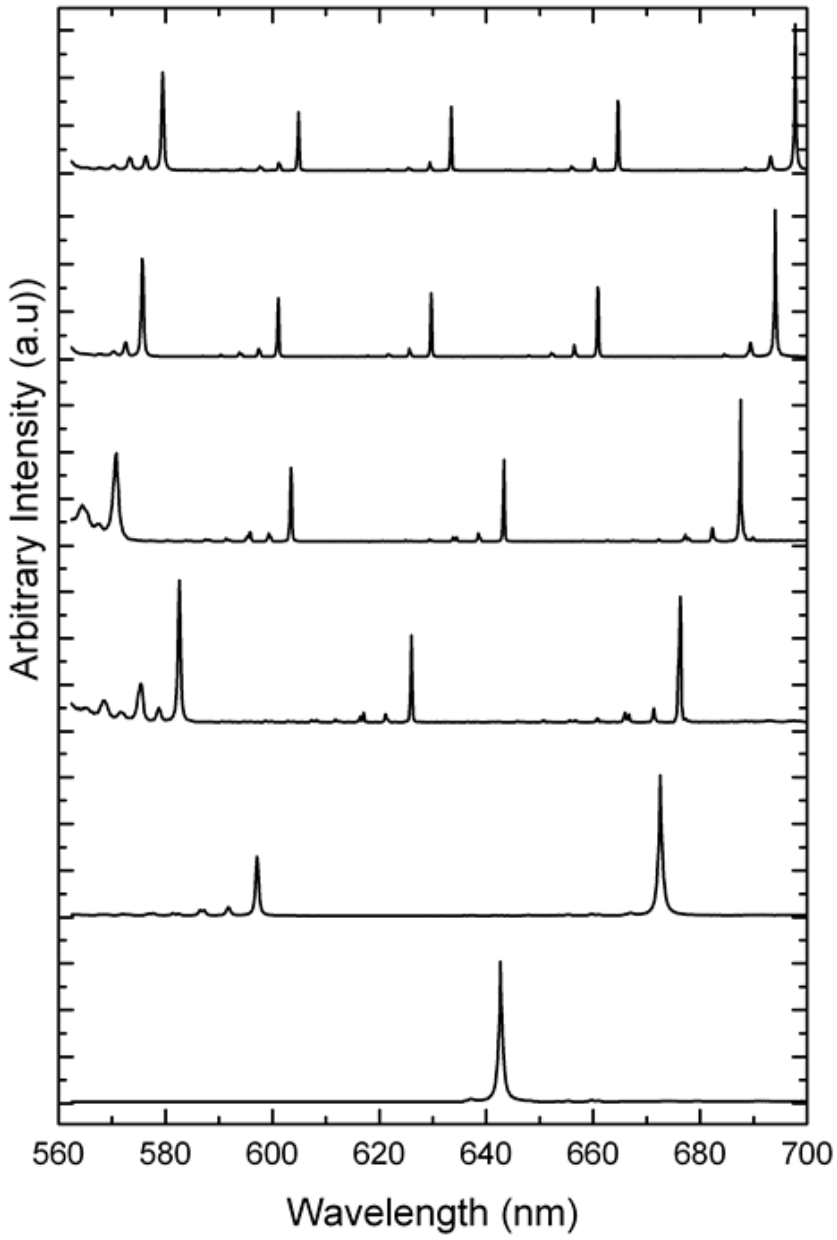

Figure 5.3.5: Sequence of spectra taken with different cavity lengths. A longest cavity length of 6.58 μm and the shortest cavity length of 2.28 μm have been obtained.

The Q factor was realised by fitting the data points with a Lorentzian line shape and using the FWHM of this fit. A Q factor of 6410 was measured with a FWHM of $0.10 \pm 2.5 \times 10^{-2}$ nm at the resonant wavelength of 640.8 nm (equation 2.5 and figure 5.3.6 (a)). A closer investigation showing a deconvolution with spectral response was performed, corresponding to a *sinc* function in figure 5.3.6(b). The spectrometer's grating with 1200 grooves/mm was used, which has a resolution limit of about 0.05 nm. Therefore the transmission lines cannot be fully resolved when the narrowest linewidth was getting close to the spectrometer's resolution limit. As discussed, the Q factor was calculated by fitting a Lorentzian curve to the experimental data with respect to different cavity lengths (figure 5.3.5). Figure 5.3.7 shows the plot of Q factors against cavity lengths, indicating a general increase trend in Q factor as the cavity length is increased. The highest Q factor of 7000 was achieved at L= 6.58 μm. From the discussion in chapter 2, the Q factor would be expected as a linear increase with cavity length. However, the Q factor at cavity length of 2.74 μm is relatively lower than expected, which can be attributed to spectral drift. This can be realised that mirrors were already in contact at the edge when L= 2.74 μm, and therefore the cavity mode had been stabilised. Nevertheless, the drift had to be taken in account when the substrates suddenly were out of contact. Even though the efforts on minimising the drift were clearly taken before the spectra of cavity mode were recorded, it was hardly to be removed entirely. This can be another error source for calculating the Q factor. The diagram showing finesse as a function of cavity length is plotted in figure 5.3.8. It is noted that the finesses deceases as the cavity length increases.

As mentioned above, the transverse modes can be excited when the light illumination is misaligned with respect to the cavity. Figure 5.3.9 shows a resonant wavelength at 643.5 nm with several transverse modes. The splitting of the second order transverse modes ($m + n = 2$) was observed, whilst the first order transverse showing no splitting. This degeneracy is formed of Hermite-Gauss transverse modes, as the cavity is not radially symmetric but has a distinction between horizontal and vertical axes.

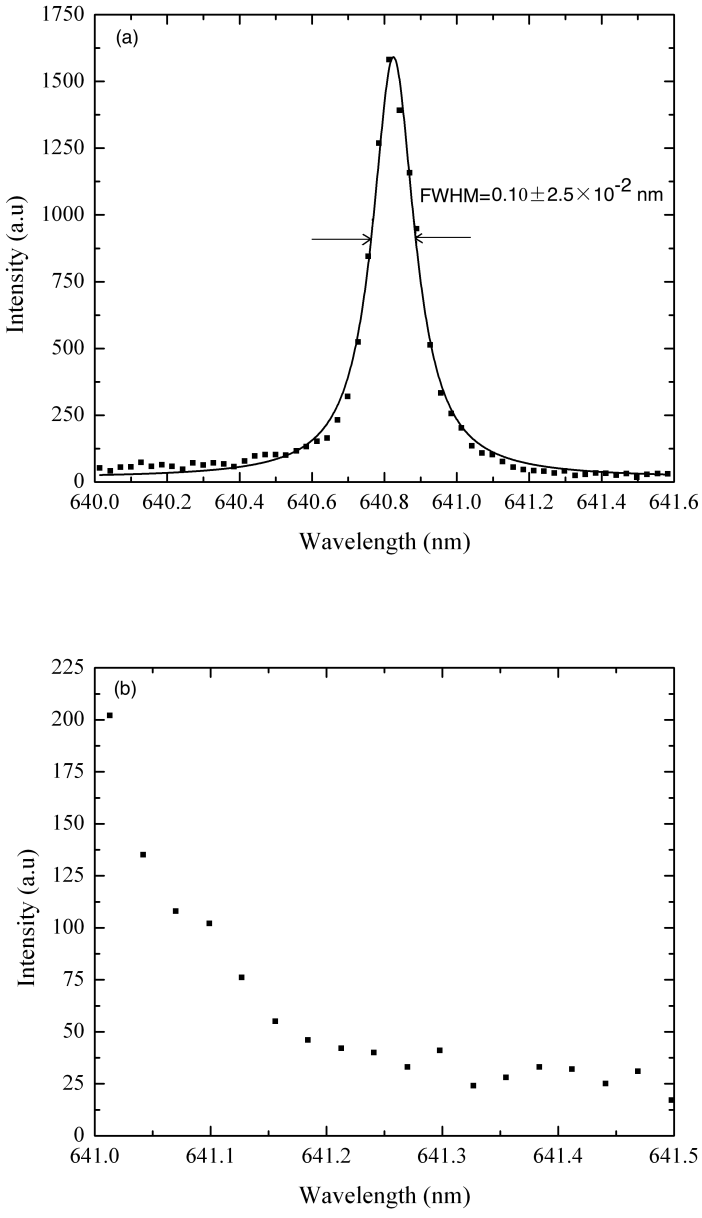

Figure 5.3.6: (a) Lorentzian fit to a cavity mode with a 40 nm FSR. The FWHM is $0.10 \pm 2.5 \times 10^{-2}$ nm at resonant wavelength of 640.8 nm (b) A closer investigation of figure 5.3.6(a), showing a deconvolution with spectral response with a *sinc* function.

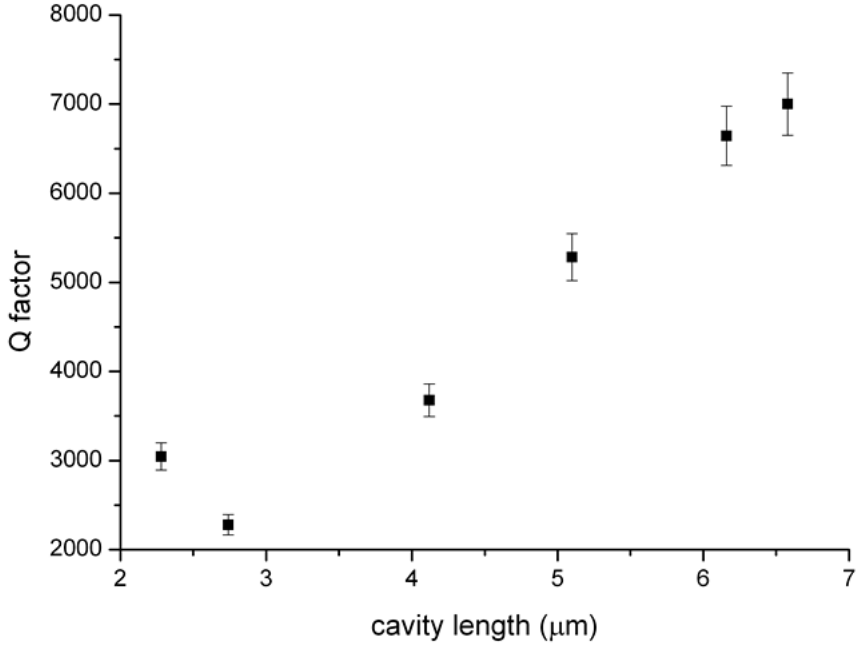

Figure 5.3.7: The Q factors for every longitudinal mode as the cavity length is increased (corresponding to data in figure 5.3.5)

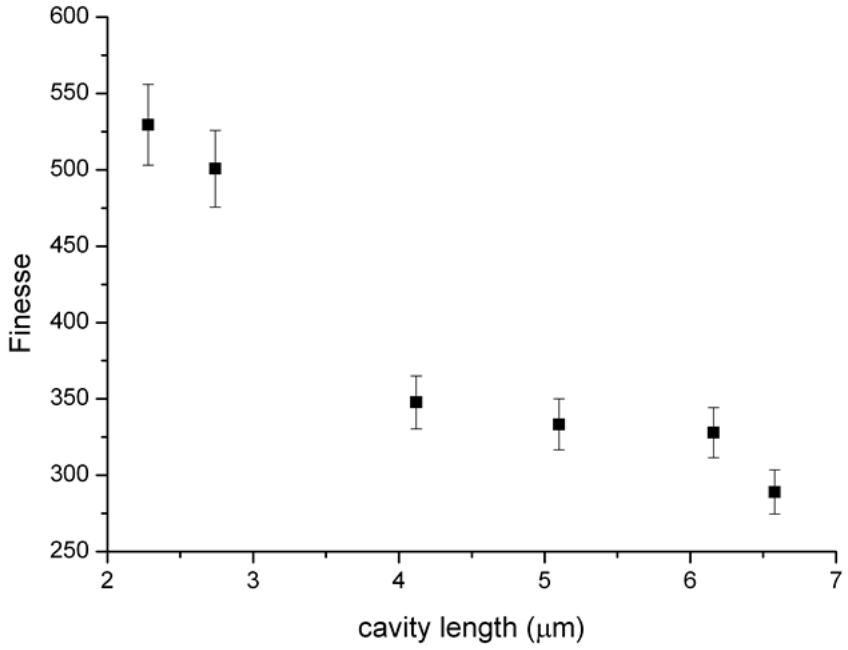

Figure 5.3.8: The finesse for every longitudinal mode as the cavity length is increased (refer to data in figure 5.3.5)

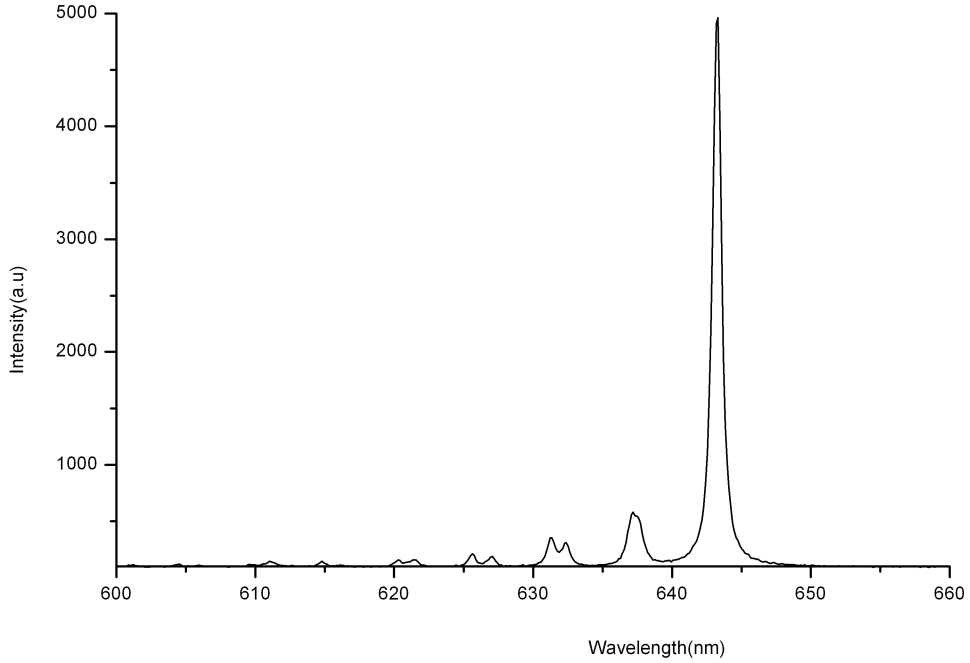

Figure 5.3.9: spectrum obtained from cavity displaying splitting of the transverse modes at 633 nm, 626 nm and 621 nm. The resonant wavelength is centred at 643.5 nm.

5.4 Summary

This chapter presented the realisation of a tunable open access microcavity. The highest Q factors of 7000 has been achieved with a finesse of ∼530. These microcavities have shown good tunability in degrees of freedom so that they are versatile to be applied in various experiments. The experiments of coupling colloidal nanocrystals using these microcavities will be described in the next two chapters.

Chapter 6

Nanocrystals in Optical microcavities

6.1 Introduction

This chapter provides results from coupling colloidal semiconductor nanocrystals, known as QDs, to microcavities. The description of the experimental arrangements will be first discussed, followed by sections where the results will be presented. The measurements will begin with QDs-microcavity coupled system, and then a single nanocrystal in a microcavity will be demonstrated. Previous work has shown the solution-based single nanocrystal-microcavity and Purcell effects [16]. In this thesis, however, the nanocrystal solution was spin cast on the mirror instead of solution-based system, providing fixed nanocrystals in position. Also, a new design of cavity holder for single nanocrystal-microcavity will be described, which gives more degrees of freedom for nanocrystals.

6.2 Experimental setup

A schematic of the epifluorescence microscope used for collecting PL from nanocrystals is shown in figure 6.2.1. For nanocrystals excitation, this system was equipped with a PicoQuant laser (λ = 473 nm) with a power on the QDs-microcavity of up to 20 μW. The same objective lens with 20x magnification and numerical aperture of 0.4 was used to collect PL from nanocrystals that was then guided to the spectrometer. Instead of using a fibre-coupled system, the free-beam coupling was set up, allowing good mode

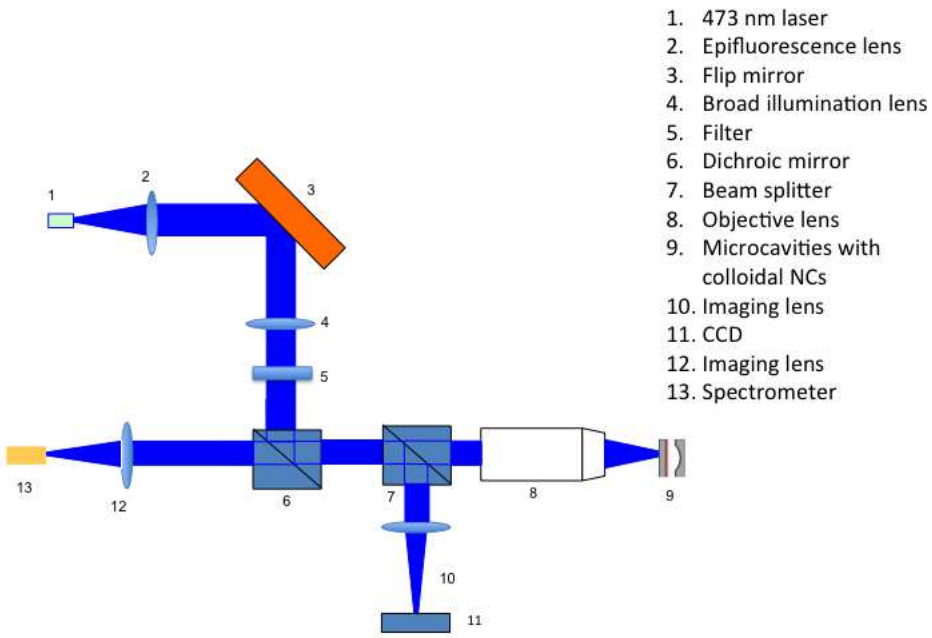

Figure 6.2.1: Schematic of experimental setup used to obtain photoluminescence from nanocrystals in microcavities.

matching to the cavity mode. A broad illumination lens was mounted such that it could be switched in and out of the optical path with no realignment required. Such lens defocusses the laser and reduces the laser intensity; this is particularly critical for the semiconductor nanocrystals as they can undergo photo-bleaching by high (focused) laser intensity. Characterisation was then performed using broad illumination and a CCD was incorporated to record the data.

The design for optical setup of the cavity holder has been developed by introducing an $x - y$ translation mount, which allows the microcavities to be tuned in three dimensions. This modification can be extremely important due to the challenges of coupling a single QD to a resonant cavity mode. As in the cavity holding schematic of figure 6.2.2 these demonstrate that spatial tuning is achieved by moving the planar mirror in the lateral plane; the bottom mirror can also be tuned spectrally using a manual z actuator. In order to get two mirrors as parallel as possible, a kinematic was used for the featured mirror. The final construction of the setup involved a lens tube connecting the kinematic and the z positioner. The purpose of this design was to place white light source so that it could back-illuminate the cavities and allowed imaging the cavities using a webcam to

assist in the spatial alignment procedures. The essential importance of transmission white light was realised for single nanocrystals sensing since the presence of single nanocrystals in a microcavity could not be guaranteed. By illuminating the cavities with white light source, the resonant cavity modes could be achieved by spatial and spectral tunings. Once a nanocrystal is coupled to a cavity mode, its PL spectrum would be measured.

The colloidal semiconductor nanocrystals used in this work were CdSe/ZnS supplied by eBioscience. They are designed to fluoresce at 640 nm, which is comparable to the maximum reflective region of the dielectric stacks in use. In order to fabricate thin QD films, polymethylmethacrylate (PMMA) polymer composite and chloroform ($CHCl_3$) were used as the embedding matrix and the solvent for QDs. PMMA was chosen for transparency in the visible spectral range and a $1wt\%$ of PMMA in $CHCl_3$ was the most appropriate concentration to produce a film of good quality. For the initial measurements of QDs-microcavity coupled system, a solution of nanocrystals and $CHCl_3$ in a ratio of $1:400$ was achieved that was then simply spin cast on the top planar mirror.

6.3 PL spectra from nanocrystals coupled to optical microcavities

In this section the emission spectra from nanocrystals are presented. Prior to taking PL measurements from cavity coupled nanocrystals, the emission spectrum from nanocrystals in free space was first recorded as a comparison. Ensemble PL measurement taken from nanocrystals out of microcavity is shown in figure 6.3.1. As expected, it shows an inhomogeneous broadening due to different nanocrystal sizes, which can be fitted with a Gaussian fit. The maximum intensity occurs at 640 nm with a FWHM of about 24 nm. Figure 6.3.2 shows a spectrum demonstrating the cavity modes illuminated by PL with a resonant wavelength at around 640 nm. Longitudinal and transverse modes are observed which give rise to Hermite-Gauss mode structures. The longitudinal modes (TEM_{00}) are seen at 580 nm and 655 nm, while transverse TEM_{mn} modes with $m + n = 1, 2, 3$ are visible at short wavelength side of longitudinal mode at 655 nm. A FSR of 75 nm can

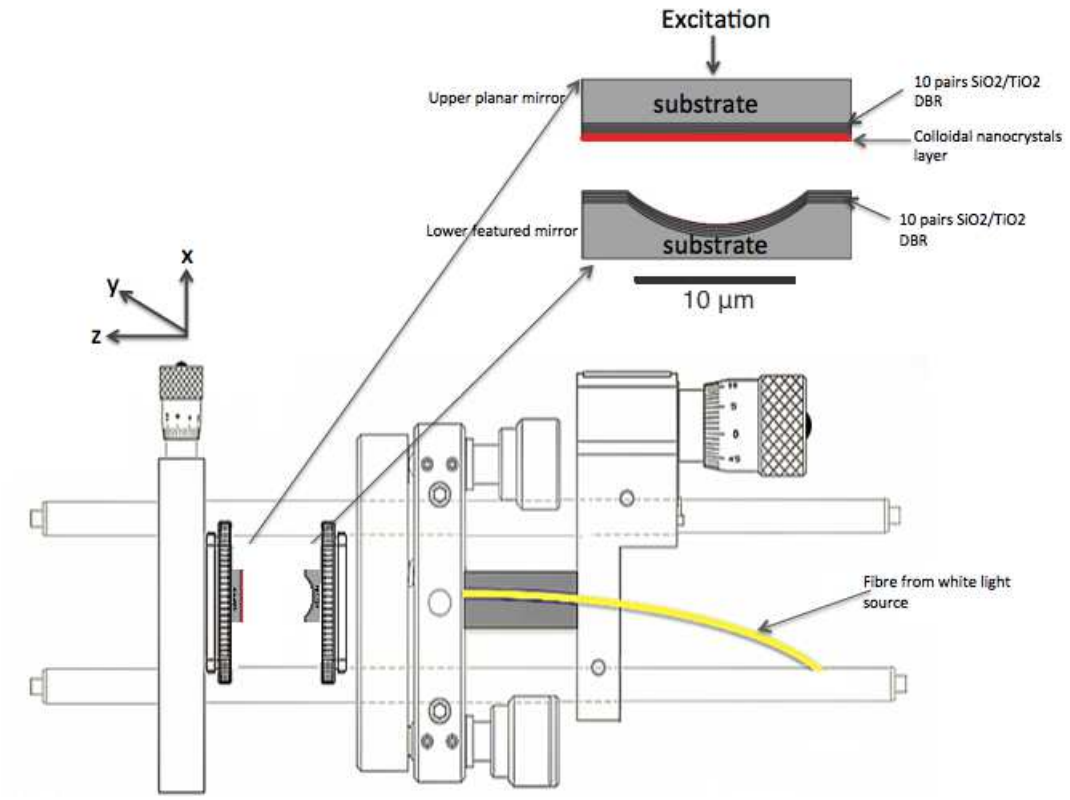

Figure 6.2.2: Schematics of cavity holder and half symmetric cavity. The bottom mirror coated with CdSe/ZnS quantum dots was mounted with z positioner and a kinematic actuator and the curved template was mounted on the $x - y$ positioner. White light source was back-illuminated through microcavities.

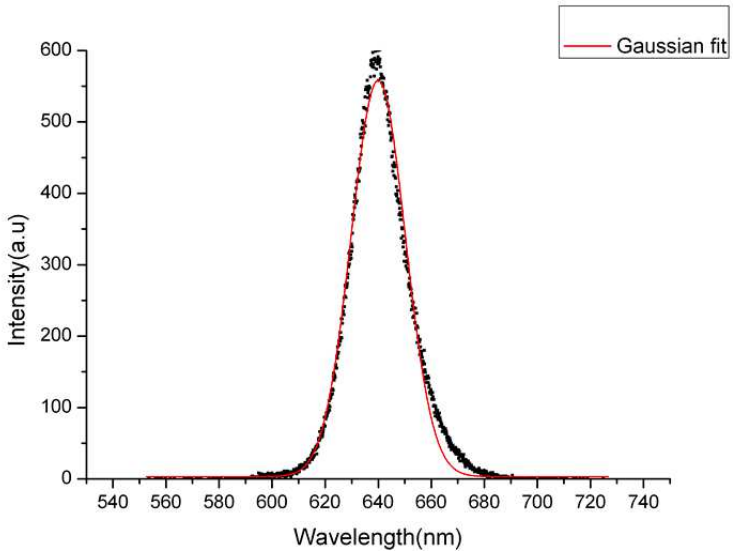

Figure 6.3.1: Emission spectrum of nanocrystals in free space, fitted with Gaussian fit. The inhomogeneous broadening with a FWHM of 24 nm shows different particle sizes of the nanocrystals.

be determined from the two longitudinal modes, allowing a cavity length of 2.73 μm to be calculated (see equation 5.2). The longitudinal modes would be expected to have the highest emission intensity compared to their transverse opponents. Clearly this is not the case here as emission peak is centred at 640 nm with a transverse mode ($m+n=2$). One explanation for this can be seen from considering the background of emission spectrum of free space nanocrystals. The cavity modes seen from figure 6.3.2 are superimposed on a broad background signal arising from the nanocrystals emission, which renders the transverse modes to obtain higher emission intensity. The detail of mode structures revealed by a higher grating ($1200\,g/mm$) is presented in figure 6.3.3. Transverse modes with $m+n=1$ can be seen at 643.2 nm, 644.1 nm, 648.6 nm and 649.3 nm, along with the Hermite-Gauss mode structures and a corresponding transmission spectrum in figure 6.3.4. By comparing the white light illumination, the PL from colloidal nanocrystals excites more transverse modes. Since the cavity was illuminated over a large area with nanocrystals, better coupling of photons to the cavity mode was achieved. On the other hand, the cavities were only illuminated over a small angle with NA=0.25 by the white light excitation.

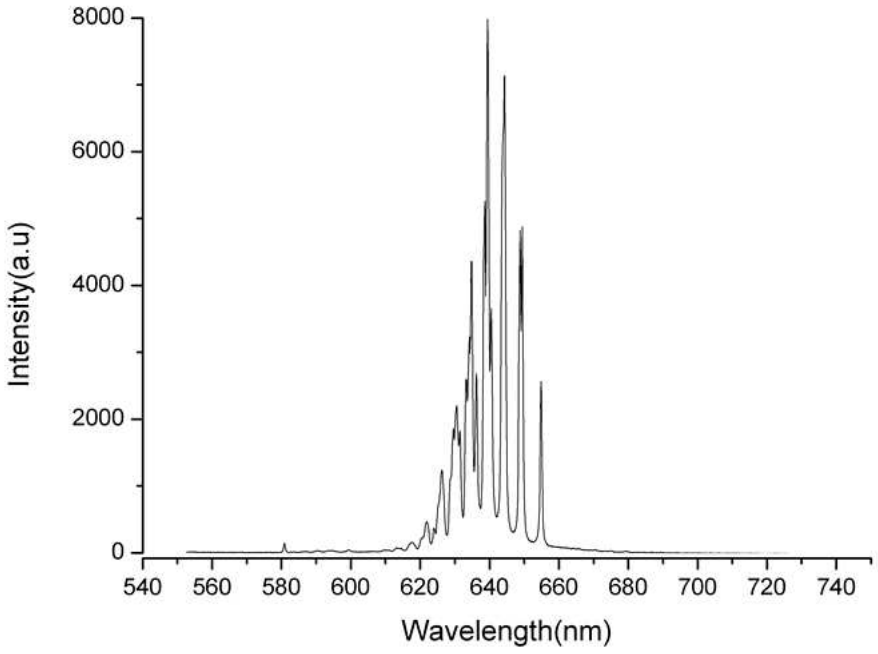

Figure 6.3.2: Emission spectrum of nanocrystals inside a microcavity at a resonant wavelength of 640 nm (L=2.73 μm and β= 25 μm). Measurements were taken at 298K.

If the nanocrystals are in resonance with the cavity mode, a spectrum of which is illustrated in figure 6.3.2. When the cavity is spectrally tuned, a 'doughnut' cavity mode is observed that is due to an interference of higher order transverse modes, shown in figure 6.3.5. In this case, the primary longitudinal mode was not perturbed but the lateral modes from the emissive area of nanocrystals had more background PL contributing to the signal, which leads to less mode structures to be identified. Hermite-Gaussian TEM_{10} and TEM_{01} modes disappeared so that TEM_{10}* was formed with a 'bagel' mode. It is noted that the PL intensity decreases as the cavity is detuned with a red shift of its PL. Since $E = hc/\lambda$, the longer resonant wavelength results in a lower transverse energy (E = 1.91 eV at λ = 649 nm), leading to less lateral confinement of off-resonance cavity modes.

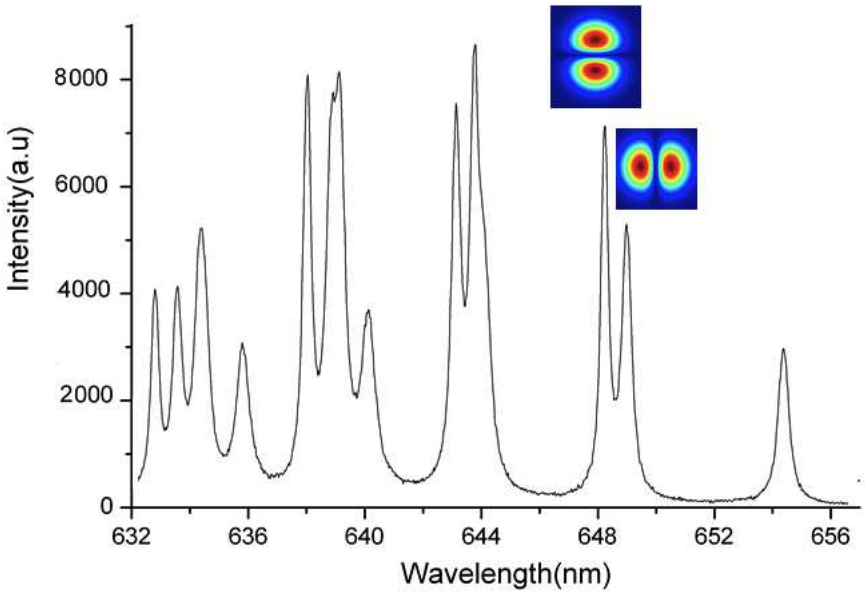

Figure 6.3.3: Spectrum obtained from cavity-coupled nanocrystals in the high resolution of 1200 grooves/mm, displaying pronounced splitting of the transverse modes. FDTD diagrams of TEM_{10} and TEM_{01} transverse modes are highlighted (Acknowledging P. Dolan for MATLAB code).

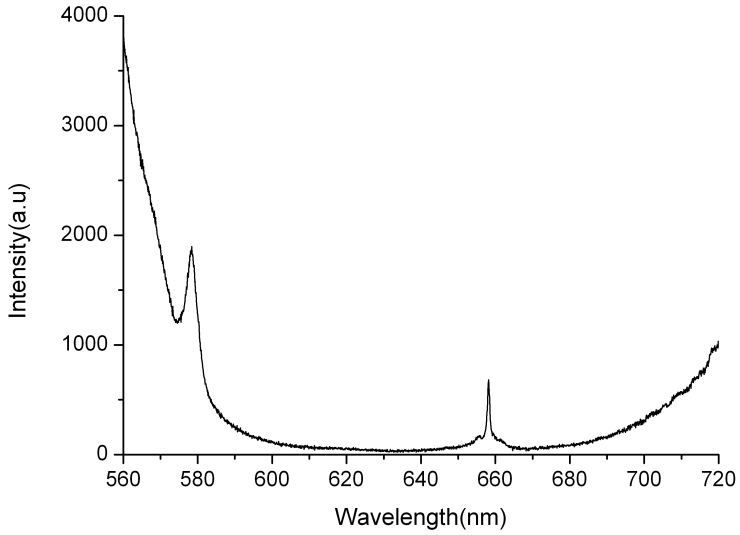

Figure 6.3.4: Spectrum taken from transmission experiment, which corresponds to data in figure 6.3.3.

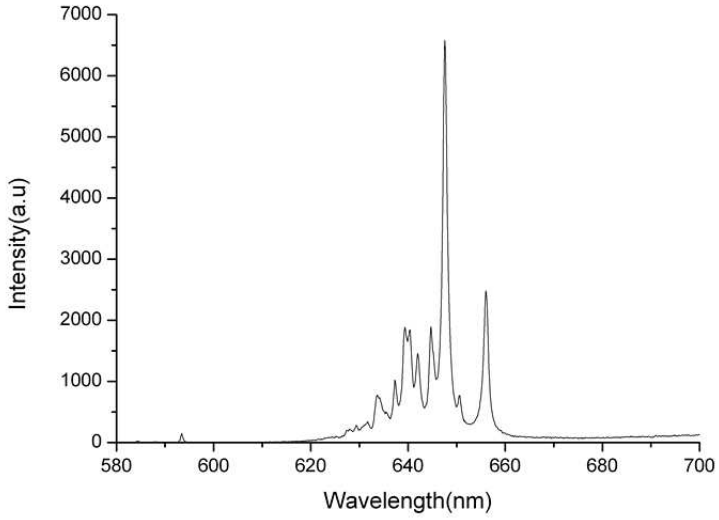

Figure 6.3.5: Emission spectrum from nanocrystals coupled to a detuned cavity mode. A 'doughnut' cavity mode is formed due to an interference of higher order transverse modes.

6.4 Coupling a single nanocrystal to a cavity

In this section the measurements of emission from a single nanocrystal into a cavity mode are presented. With no modification of the experimental setup and cavity mirrors, a series of dilution of the colloidal nanocrystal solutions were carried out until a low density of 0.02 QD/μm^2 was obtained (see figure 6.4.1).

Spectra from a single nanocrystal in free space and within the cavity are demonstrated in figure 6.4.2. The upper plot shows the spectrum for a single nanocrystal out of the microcavity at room temperature, whilst the lower one reveals the emission profile from a single QD in a cavity. Figure 6.4.2(a) shows PL from a single nanocrystal having a homogeneous Lorentzian curve with a FWHM of 20 nm. This can be contrasted with the spectrum in figure 6.3.1, whose linewidth has inhomogeneous broadening with a width of 24 nm. Moreover, the FWHM of the illuminated cavity modes in figure 6.4.2 (b) shows a substantial decrease compared to the linewidth of the single nanocrystal in free space. At resonant wavelength an increase in the photon count rate has been characterised in the cavity with respect to the uncoupled one. The longitudinal mode TEM_{00} is excited at 640 nm, followed by transverse modes ($m + n = 1\,and\ 2$) at 633 nm and 638 nm, respectively. A corresponding transmission spectrum was taken from the same region of

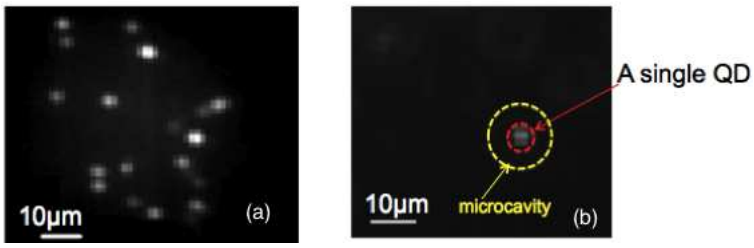

Figure 6.4.1: (a) An image taken from single nanocrystals in free space with a 60x magnification objective lens. Figure 6.8 (b) An image of a single nanocrystal coupled to a cavity with a 20x magnification objective lens.

interest by switching on the back illuminated white light without PL excitation (see figure 6.4.3). A broadened mode at round 620 nm is displayed in figure 6.4.3, highlighting the weak coupling to the cavity mode at this wavelength. Therefore no clear features of mode structure can be observed in figure 6.4.2(b) at 620 nm.

The radius of curvature can be calculated from the separation between two subsequent transverse modes (see equation 2.12). It is noted that there is considerable discrepancy between measured radius of curvature (47.7 μm) and theoretical one (25 μm), which may be affected by the fabrication process. The longitudinal mode number q and transverse modes (m, n) have been highlighted in figure 6.4.2 (see equation 2.11). Due to the mode degeneracy, electromagnetic fields vary with transverse modes at different wavelengths in the cavity. The longitudinal mode number becomes smaller as the cavity length decreases. In the spectrum of single dot PL the smallest longitudinal mode number of 9 was achieved.

In order to confirm the PL was from a single nanocrystal in the cavity, a time trace of the cavity coupled emission spectrum for 100 seconds was recorded shown in figure 6.4.4. This reveals the fluctuation in the mode intensity with time, which can be attributed to the phenomena of single quantum dot photoluminescence intermittency. This characteristic can be credited to Auger relaxation process (see section 2.1.2), which leads to non-radiative recombination mechanisms. With a closer inspection in the time trace in figure 6.4.4, intensity fluctuations in different cavity modes are correlated, verifying that nanocrystal blinking is from a single nanocrystal photoluminescence. However, if the intensity fluctuations are not correlated with cavity modes, the presence of a second nanocrystal can be seen in the time trace in figure 6.4.5, along with its emission spectra.

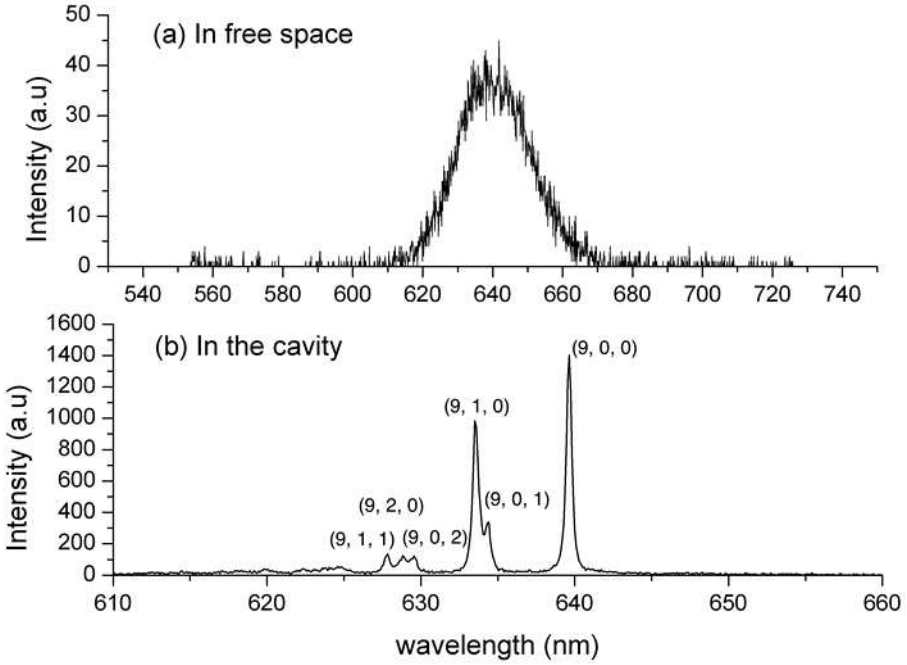

Figure 6.4.2: (a) Emission spectra obtained from a single nanocrystal in free space with a FWHM of 20 nm and (b) a single nanocrystal in the cavity with a cavity length of 2.77 μm at room temperature with a power of 19.4 μW.

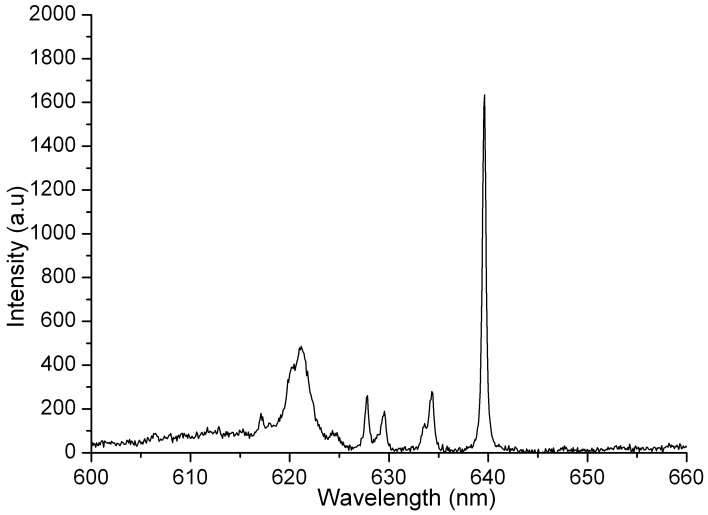

Figure 6.4.3: A corresponding transmission spectrum taken from the same region of interest in figure 6.4.2 (b). A broadened mode was observed at around 620 nm due to weak coupling to the mode at this wavelength.

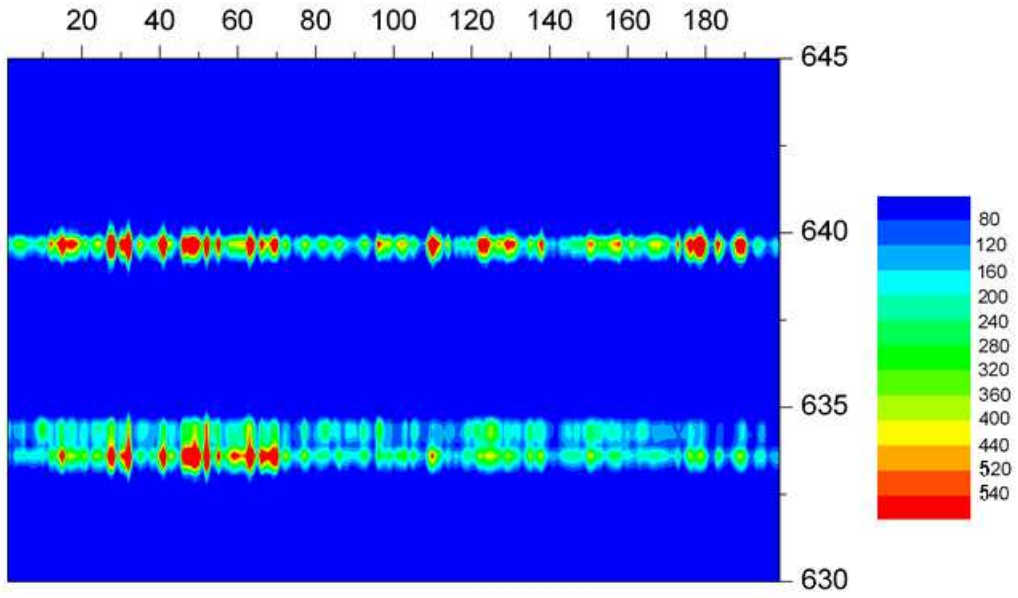

Figure 6.4.4: A time trace of a single nanocrystal in the microcavity, showing the fluorescence intermittency of the nanocrystal with an integration time of 0.5s. The intensity fluctuations in different cavity modes are correlated, which confirms that nanocrystal blinking is from a single nanocrystal photoluminescence.

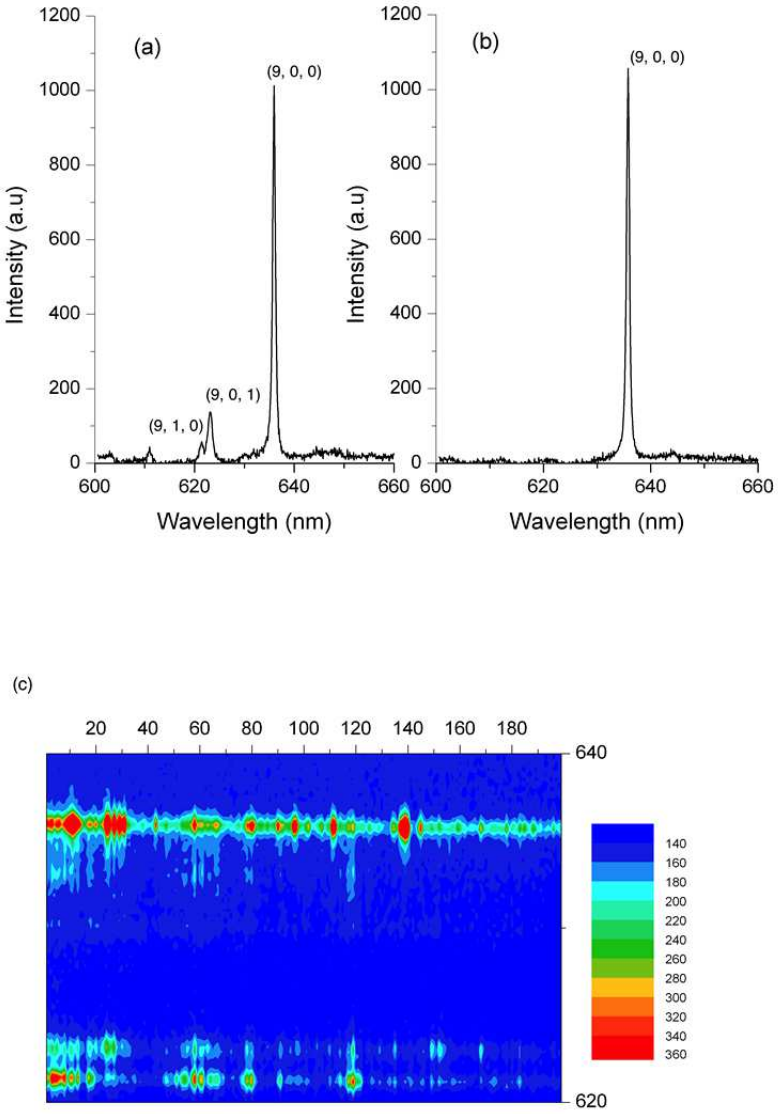

Figure 6.4.5: (a) spectrum of single dot PL at frame number 10 (b) spectrum of single dot PL at frame number 140 and (c) A time trace of a single nanocrystal in the microcavity shows that the intensity fluctuations are not correlated with cavity modes with an integration time of 0.5s.

Figure 6.4.5 (a) shows the PL spectrum of single nanocrystal with a resonant wavelength of 636 nm in 5 s (frame number 10), the longitudinal mode number q and transverse mode TEM_{10} have been established. Figure 6.4.5 (b) obtained from the frame number of 140 highlights that the nanocrystal is only coupled to a longitudinal mode; this is a remarkable result because this is the first time that a single mode emission has been observed in small cavities at room temperature. These spectra suggest that a second nanocrystal might be in the cavity that contributes to the PL emission. A further proof in figure 6.4.5 (c) shows the intensity fluctuations in the cavity modes are not correlated.

Having discussed the cavity modes from spectral information, it is now possible to investigate the control of the spontaneous emission from a single nanocrystal by the presence of the microcavity.

6.5 Summary

In this chapter, a single nanocrystal coupled to a microcavity has been demonstrated. More importantly, the PL spectrum of single mode emission has been observed, suggesting that such microcavity coupled nanocrystals system can be potentially used in SPS.

Chapter 7

Time-Resolved Photoluminescence of a single nanocrystal in a microcavity

7.1 Introduction

This chapter will display several time-resolved photoluminescence measurements, highlighting the implications of using open access microcavities to modify the spontaneous emission rate from nanocrystals.

7.2 Modified lifetimes by spectral tuning

In order to measure the lifetime of a single nanocrystal inside the cavity, a single photon avalanche diode (SPADs) was used, which could detect low intensity signals with a timing resolution of about 500 ps. The operation of the SPADs is based on a $p-n$ junction reverse-biased at a voltage just above the breakdown voltage. This means a single photon triggers a current pulse in the mA region that can be easily counted. A time-correlated single-photon counting (TCSPC) was applied to record the duration between the arrival of the trigger pulse from a pulsed laser in respect to the arrival time of the next pulse from the SPAD, which results in a histogram of photon arrivals as a function of their time. This technique used for detection of photons of a periodical light signal is known as time-resolved photoluminescence or TRPL. The experimental setup is depicted in figure

7.2.1, and data was measured with a 100 ps duration excitation pulse and a 900 ps overall timing resolution. Instead of collecting light by the spectrometer, the flip mirror was implemented on the path where light was reflected and guided onto the fibre coupled SPAD port. Special care was taken to keep the excitation intensity under 1 μW to avoid the generation of biexcitons that can result in Auger-limited decay in a few picoseconds. Figure 7.2.2 illustrates the fluorescence decay taken from a single nanocrystal in the smallest cavities (L=1.53 μm), compared to nanocrystals outside the cavities, but in the similar operating environment at room temperature. The free space emission shows approximately single exponential decay of lifetime 14 ns, which is comparable to the last publication [16]. The cavity coupled single nanocrystal, however, clearly reveals biexponential decay with a shorter lifetime than the uncoupled one. The decay rate with the best coupling to the modes, where nanocrystals located close to the field anti-nodes, can be seen from considering the first 20 ns of the decay by the linear fit. Since the equation for an exponential intensity decay is given by $I = I_0 e^{-t/\tau}$, the decay rate $(1/\tau)$ can be determined from the log-linear plot. With the best fit in the first 20 ns, the fitted cavity coupled decay rate relative to the free space decay rate, γ'/γ_0, of 1.72 is obtained along with decay rates of 0.043 ns^{-1} and 0.025 ns^{-1}, respectively. The series of TRPL data were then recorded by changing the cavity length (i.e spectral tuning). The expression of mode volume of each cavity can be calculated in terms of its radius of curvature and cavity length, shown in equation 7.1.

$$V = \frac{\lambda L^2}{4n}\sqrt{\frac{\beta}{L} - 1} \tag{7.1}$$

Where $n = 1$ (in air), L is cavity length, λ is the resonant wavelength and β is the radius of curvature. Rather than use linear fit for first 20 ns of the decay rate, the best route to match the decay is to use biexponential decay fit for each cavity. For a biexponential equation four fitting parameters, τ_1, τ_2, A_1 and A_2 can be found where τ's are lifetimes and A's are amplitudes. A biexponential fit is depicted in equation 7.2. By plotting each of these four parameters as a function of mode volume, useful information will be provided which can be used to determine if any Purcell enhancement has occurred

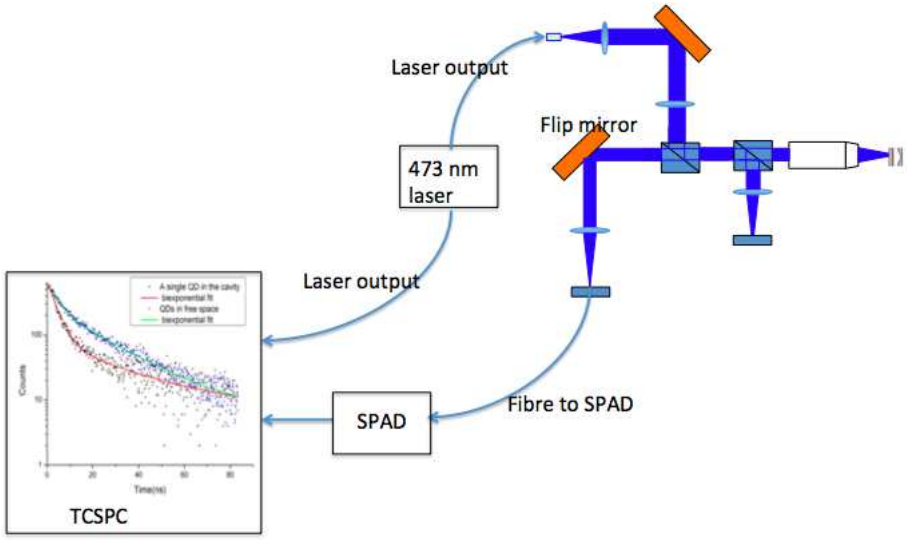

Figure 7.2.1: Schematic of the experimental set-up for time-resolved photoluminescence experiments.

shown in figure 7.2.3- 7.2.6.

$$I = I_0 + A_1 e^{-t/\tau_1} + A_2 e^{-t/\tau_2} \tag{7.2}$$

Where t is time constant and I_0 is the initial intensity at $t = 0$.

Figure 7.2.3 and 7.2.4 show the plots of mode volume against the lifetime t_1 and t_2. It is highlighted that the t_2 gets longer for small cavities as t_1 gets shorter. Recall to the Purcell equation in equation 2.21, the Purcell factor is expected to increase as the mode volume is decreased. However, the t_2 component in figure 7.2.4 does not agree with the theoretical predictions, which leads to further analysis of decay rate that will be discussed in the following section.

7.3 Analysis of spontaneous emission rate

According to figures from 7.2.3 to 7.2.6, the experimental decay data reveal that a change in Purcell effects can only be observed once the mode volume is under 4 μm^3 with the maximum modified decay rate at V=1.75 μm^3. The mode volume is noticeably larger compared to the published paper [16]. It is acknowledged that the previous work included some field penetration into the mirror with a higher refractive index of 1.4.

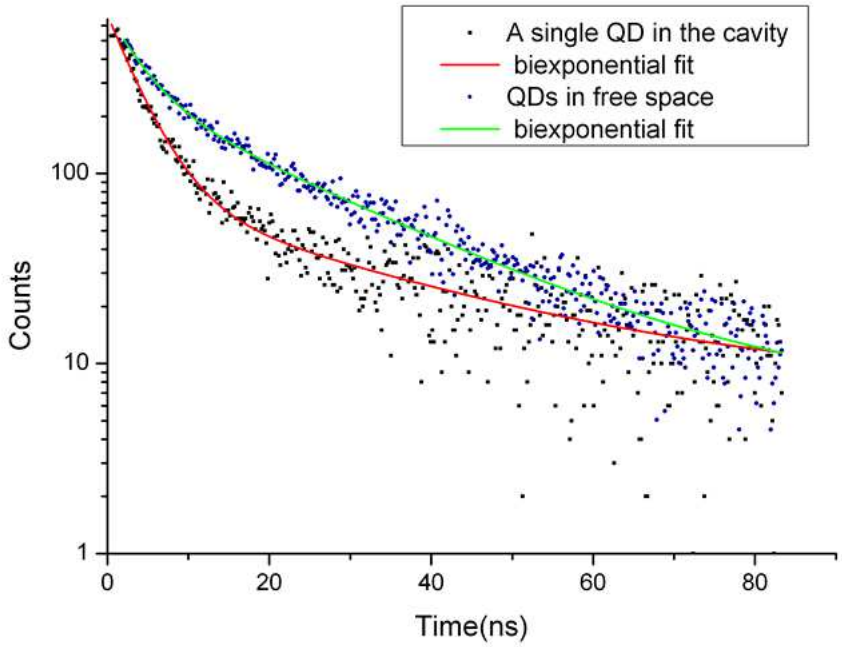

Figure 7.2.2: The semi-logarithmic plot of time resolved photoluminescence histograms for free space emission (blue dots) and cavity coupled emission (black dots), fitted with biexponential fit.

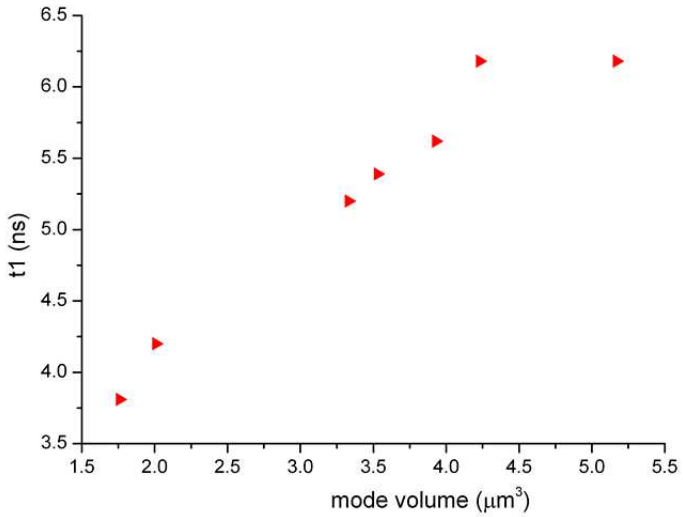

Figure 7.2.3: The plot of lifetime t_1 as a function of mode volume. The lifetime gets shorter as the mode volume is decreased. The shortest lifetime of 3.75 ns was observed for the smallest cavity of 1.53 μm.

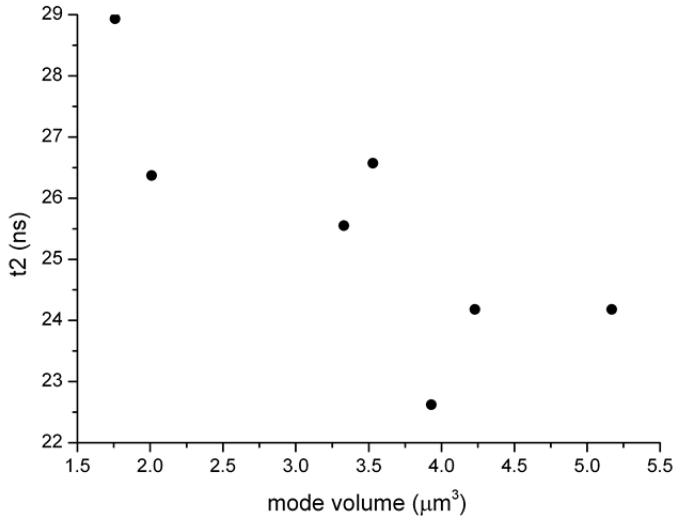

Figure 7.2.4: Plot of lifetime t_2 against cavity volume showing longer lifetime t_2 for small cavities. This directly contradicts the expression of Purcell factor enhancement. It is hypothesized that a second nanocrystal may be present that is off-resonance with the cavity mode.

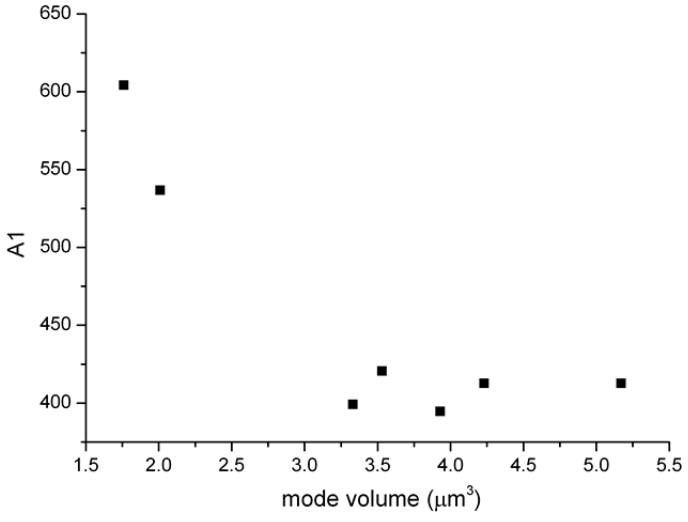

Figure 7.2.5: The plot of A_1 as a function of mode volume. For small cavities the majority of the emitted photons are funneled into the cavity mode via the Purcell effect.

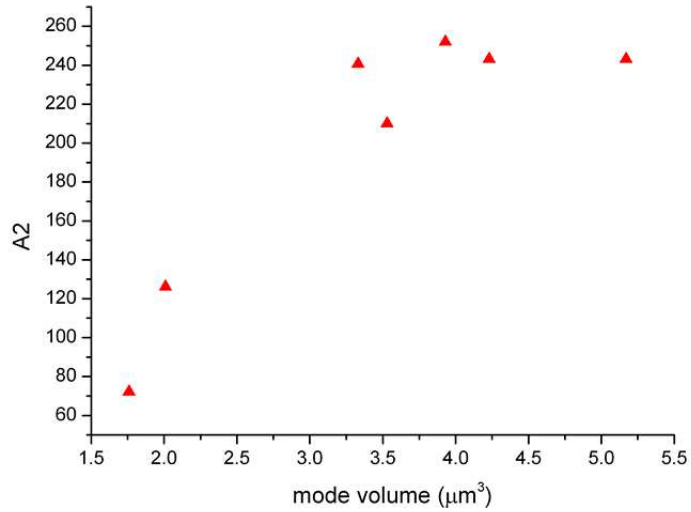

Figure 7.2.6: The plot of A_2 as a function of mode volume, highlighting large amplitude A_2 for large cavities.

Despite the fact that changes in Purcell effects have been observed through cavity volume control, the measured Purcell factors are still much lower than predicted values from Purcell expression in equation 2.21. This is due to the breakdown of the assumption in the analytic expression for the Purcell factor. As discussed in section 2.3, the effective Q factor is reduced to 45 and Purcell factor is as a function of $1/V$. Assuming that the majority of spontaneous emission from nanocrystals in free space is unperturbed by the presence of the cavity, the modified decay rate is then equal to F_p+1. For the smallest cavity the measured Purcell enhancement agrees considerably well with calculated value (equation 2.21 and equation 7.3), with F_p=0.76. Recall that the peculiar feature of t_2 component has shown in figure 7.2.4, the decay rate of cavity-QD coupled system can be modified to take three further physical factors into account: the influence of a nanocrystal coupled to several cavity modes, suppression of emission into off-resonant cavity modes and non-radiative recombination routes in the nanocrystals [16]. A more vivid schematic of the first two factors is illustrated in figure 7.3.1.

The entire expression including these three factors is described as,

$$\gamma' = \gamma_{nr} + (\sum_i F_{p,i} + \alpha)\gamma_{rad} = \gamma_0(1 + \eta(\sum_i F_{p,i} + \alpha - 1)) \tag{7.3}$$

Where γ_{nr} and γ_{rad} are the non-radiative and radiative recombination rates of the

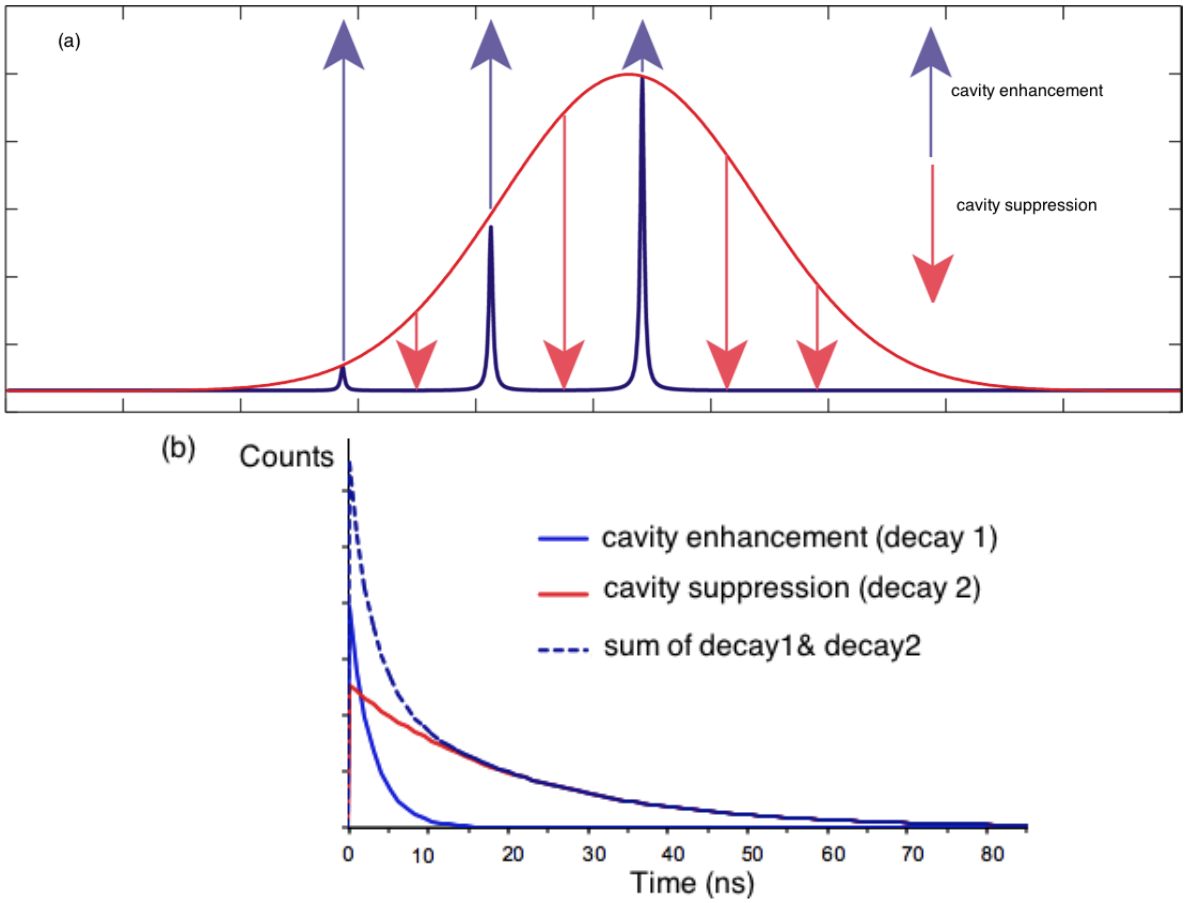

Figure 7.3.1: (a) A schematic of the on-resonant enhancement and off-resonant suppression of emitters coupled to cavities. (b) A schematic of single exponential decay 1 and decay 2, which can be summed into the biexponential decay.

excitons of nanocrystals in free space, γ_0 is the total free space recombination rate as a sum of γ_{nr} and γ_{rad}, η is the fluorescence quantum yield defined as γ_{rad}/γ_0 and α represents the suppression of emission into continuum modes ($0 \leq \alpha \leq 1$).

Here the t_2 component from a cavity-coupled nanocrystal (in figure 7.2.4) shows longer lifetimes relative to smaller cavities, resulting in a hypothesis of the presence of a second nanocrystal that is off-resonance with the cavity mode. Therefore the spontaneous emission rate is suppressed by this nanocrystal so that the biexponential decay is observed. As believed that this is the first time that the dependence of decay rate on mode volume with biexponential decay has been demonstrated using open access microcavities.

7.4 Modified lifetimes by spatial tuning

As discussed above, the Purcell expression (see equation 2.21) assumes that the QD is in resonance with the cavity mode, where is located at the exact antinode of the electric field. The open access cavities showed good tunability that was used to place a nanocrystal at the maximum of the electric field. According to my new design of the cavity holder (see figure 6.2.2) , a brand new capability of studying Purcell effect relative to different spatial detunings of cavity modes has been observed.

The same alignment procedures were used with the same methods discussed in section 7.2. Once the maximum intensity has been achieved where cavity mode was resonant with the nanocrystal, the planar mirror was tuned over several micrometres in the xy plane. Spectral resonance was maintained with no change in cavity length (i.e no spectral tuning).

Figure 7.4.1 shows the semi-log plot of the fluorescence decay relative to spatial tunings at a low excitation power ($P_{excitation}$=1 μW) and an integration time of 100s. On a log-linear plot, this should appear as a straight line as discussed. However, the altered exponential decay for the nanocrystal at resonant cavity mode does not show the perfect single exponential decay, and has several decay constants in some distinct regions. A conservative explanation is given that more than one single nanocrystal are present within the cavity. Due to different couplings of the cavity modes, a second nanocrystal may be decoupled to the cavity mode so that its spontaneous emission is suppressed.

The measured radiative lifetimes from the nanocrystal within the cavity are shown in Figure 7.4.2. Figure 7.4.2(a) presents the radiative lifetime t_1 as a function of spatial detuning in x direction. At largest detuning the radiative lifetime t_1 of 6 ns is obtained, whilst the shortest lifetime is approximately 3 ns at no detuning. Figure 7.4.2(b) illustrates the radiative lifetime t_2 becomes longer as the nanocrystal is moved spatially away from the resonant cavity mode. Figure 7.4.3 shows a series of PL intensities relative to different spatial detunings (compared to the resonant cavity modes). It can be noted that the offset nanocrystal couples more strongly to different spatial modes when the nanocrystal is laterally detuned from the maximum electric field in the cavity. The spectrum obtained

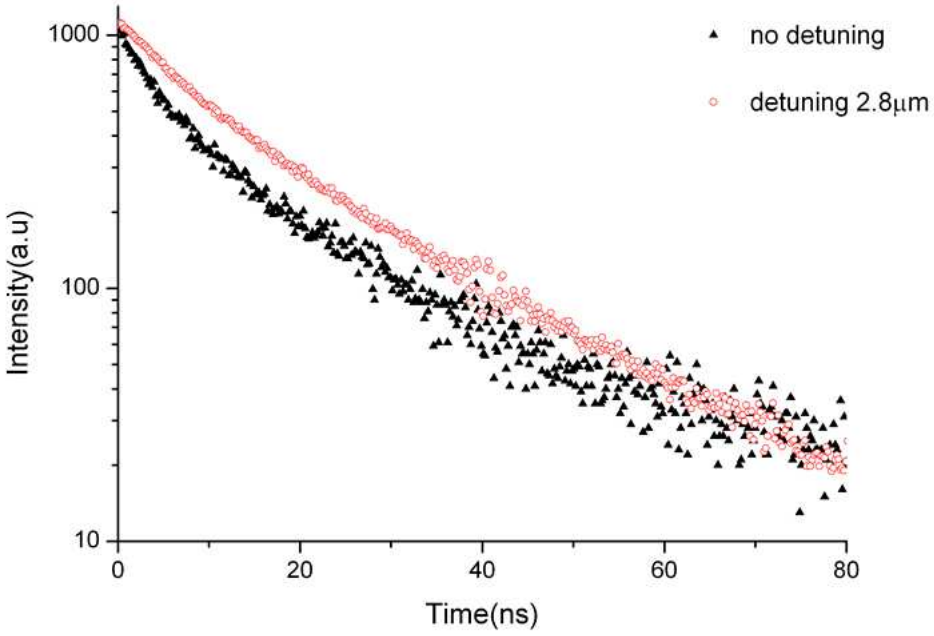

Figure 7.4.1: Time resolved photoluminescence histograms from single nanocrystal at zero detuning (black triangles) and detuning of 2.8 μm (open red circles).

from the largest spatial detuning in figure 7.4.3(g) displays the pronounced coupling of the transverse mode at 626 nm. Figure 7.4.4 illustrates the peak PL intensity of cavity coupled nanocrystal as a function of spatial detuning. These plots point out the importance of spatial tuning in the microcavity, to ensure that the nanocrystal is in resonance with the cavity mode.

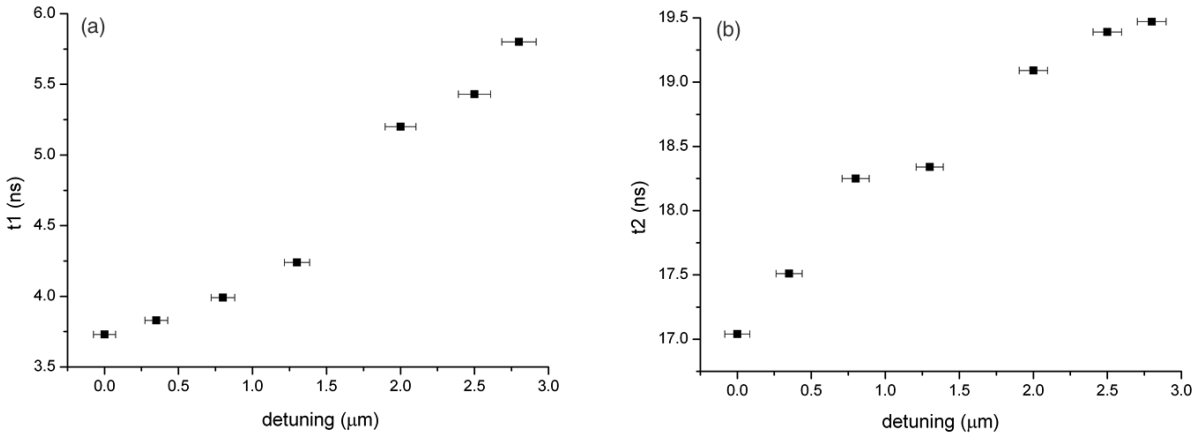

Figure 7.4.2: (a)(b) lifetime t_1, t_2 as a function of spatial detunings in x direction with an error bar of 5% in x direction.

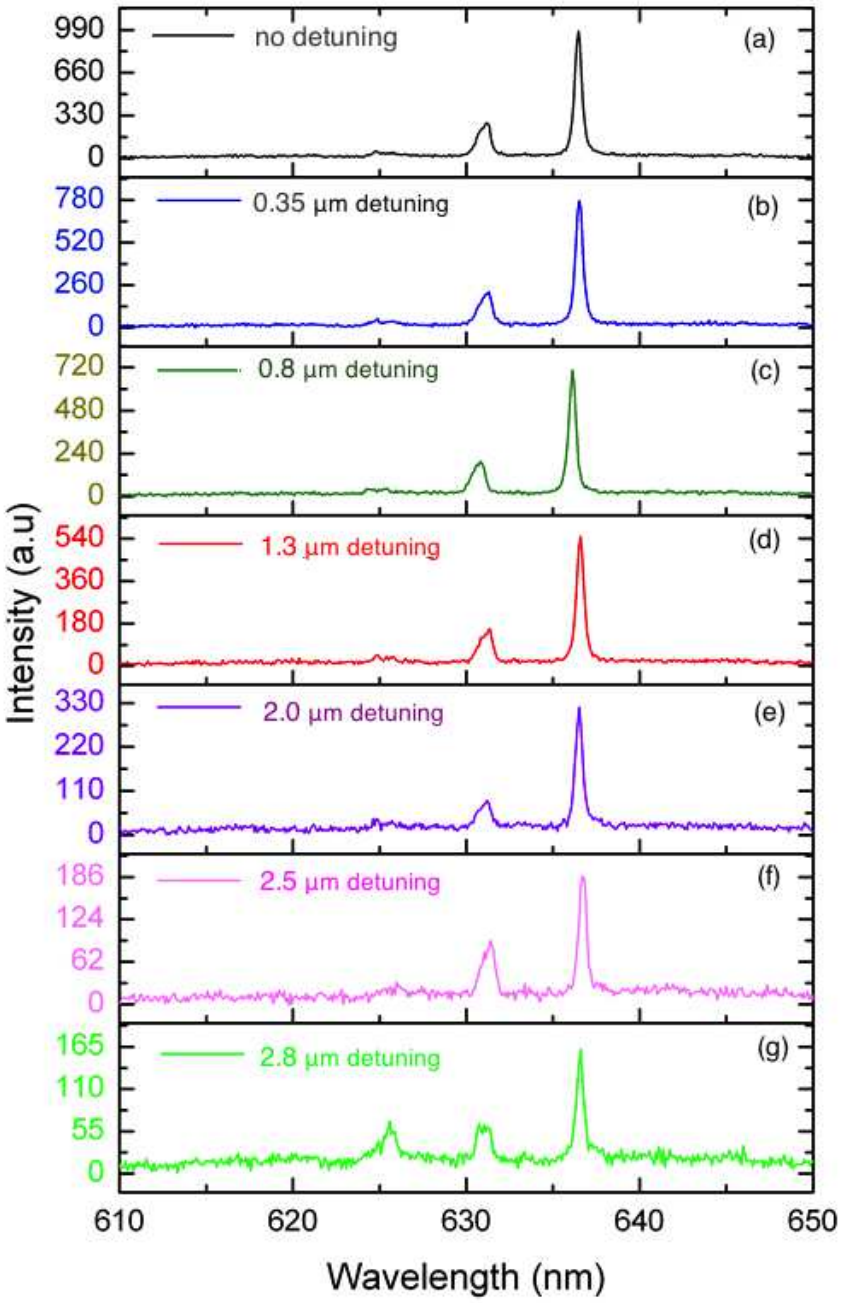

Figure 7.4.3: shows a series of intensities of coupled single nanocrystal relative to different detunings. At zero detuning, the emission spectrum from single nanocrystal is optimised with respect to x direction and y direction. The intensity reduces as the nanocrystal moves away from the resonant cavity modes and the nanocrystal couples more strongly to different spatial modes as spatial detuning is increased.

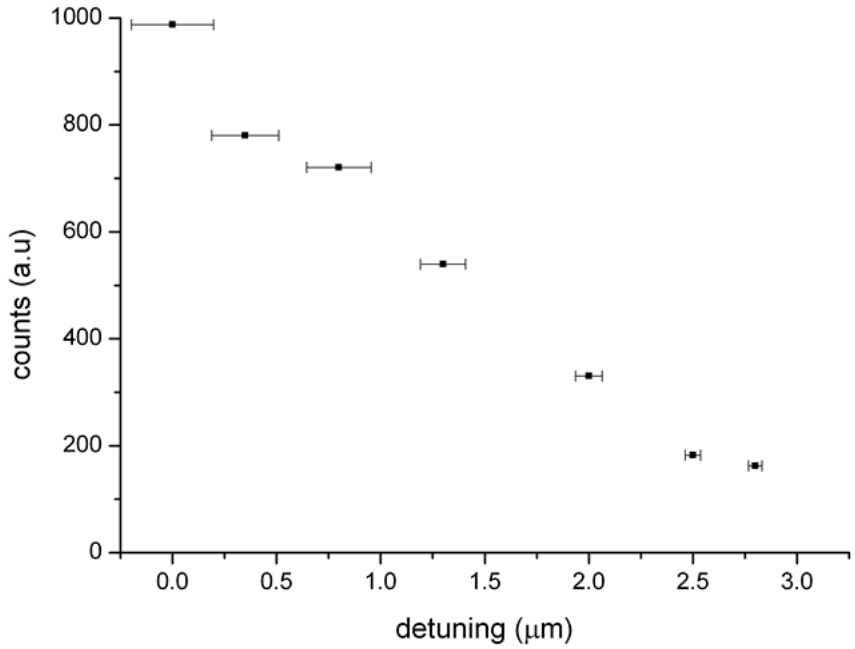

Figure 7.4.4: Peak PL intensity of cavity coupled single nanocrystal as a function of spatial detuning with an error bar of 5% in x direction.

7.5 Conclusions

In this chapter, enhancements of the spontaneous emission from CdSe/ZnS quantum dot in the microcavity at room temperature in spectral tuning and spatial tuning have been demonstrated. The importance of coupling a single nanocrystal in the resonant cavity mode using the new design of experimental setup has been highlighted.

Chapter 8

Conclusions and future work

8.1 Conclusions

The open access microcavities with hemispherical features were shown to be fully operational at room temperature. By placing single QD in such a microcavity, the PL intensity increases significantly compared to single QD in free space. More importantly, single mode emission has been achieved which can be potentially useful for generating SPS.

A single QD's radiative lifetime was also studied as a function of its spectral tuning and spatial tuning with respect to the resonant cavity mode. This highlights the importance of measuring the best coupling of single QD to the cavity mode. A Purcell enhancement of 1.72 was measured for the single QD when it was placed in the maximum electric field in the cavity using the new design of xy positioner and z positioner. The radiative lifetime of a single QD was expected to be single exponential decay. However, a biexponential feature of the QD's radiative lifetime was observed, which leads to a hypothesis of the presence of a second nanocrystal that is off-resonance with the cavity mode.

In the case of spatial detuning, the promising results have shown that the offset nanocrystal coupled more strongly relative to different spatial modes, providing the potential of studying different interactions of QD-microcavity system.

Although Purcell enhancement of cavity coupled single QD has been achieved, its radiative lifetime did not show a perfect single exponential decay. It may be attributed to the presence of a second nanocrystal in the microcavity or some unknown properties

of single QD. Therefore, further measurements need to be taken in order to test single nanocrystals.

8.2 Future work

The TRPL measurements should be taken again in the same operating conditions to test the hypothesis of a second nanocrystal in the microcavity. In addition, the correlation measurements using a Hanbury Brown-Twiss interferometer should indicate that when a single nanocrystal is coupled to a cavity mode.

One other experiment which would be extremely interesting to pursue is the spatial matching of the single nanocrystal in $\pm$ y axis relative to the resonant mode, to ensure an optimal interaction with the cavity mode.

Chapter 9

Project management

9.1 Objective

The objectives of the project have been clearly highlighted in the beginning of the thesis. There were to measure photoluminescence and radiative lifetime of a single nanocrystal coupled to a microcavity, to determine if any enhancements of spontaneous emission rate can be observed. Prior to the realisation of the targets of the project, several experimental skills including optical spectroscopy, laser handling and preparations of nanocrystal solutions were required.

9.2 Initial results

Initial work was devoted to characterising open access microcavities with no emitters in transmission experiments. Skills of using the optical kits were trained to assist in any alignment procedures. Once some decent results from transmission experiments have been achieved, the work was shifted to focus on characterisation of coupling colloidal nanocrystals to microcavities. To start with, the method of preparing solutions of nanocrystals was learned and several photoluminescence measurements from high density nanocrystals in microcavity have been demonstrated. A serial dilution of the colloidal nanocrystal solution was then carried out until the optimal concentration was obtained. Promising results from coupling a single nanocrystal to a microcavity has been achieved. In addition,

radiative lifetimes from cavity coupled single nanocrystal were also measured, showing an enhancement of spontaneous emission rate compared to uncoupled single nanocrystals.

9.3 Time management

In early Michaelmas Term, the trainings on equipment and software were carried out as well as reading the literature and learning the theories. In order to get a smooth start in this project, chances to participate in the lab work with members of the group were demanded. Also discussions with group members have assisted me in becoming more familiar with the project. Most of the equipment in this project had to be booked. The high demanding lab time therefore required a clear mind in what goals need to be achieved for each session. Despite time on the equipment being extremely restricted, it did not hinder any progress with the project.

In the first two months, main work has been devoted to optical characterisation of microcavities in transmission and photoluminescence measurements from colloidal nanocrystals in microcavities. Spectra obtained from transmission and photoluminescence measurements have shown good progress towards the final goal of single QD level.

The second term was focused on cavity coupled single nanocrystal system. By diluting solutions of colloidal nanocrystals, several different concentrations of nanocrystals have been characterised. At the same time, a new setup for single nanocrystal-cavity system was designed and built up. The $x-y$ positioner was introduced to be able to move mirrors in three dimensions, the importance of which was highlighted throughout the thesis. The first emission spectrum of a single nanocrystal in a microcavity was achieved in early April. This was followed by a series of lifetime measurements of single nanocrystal in the microcavity. Promising results from cavity coupled single nanocrystal were achieved.

9.4 Unexpected Problems

When the desirable concentration of nanocrystal solutions was obtained, the solution was spin coated on the planar mirror for photoluminescence measurements. It was thought

that the photoluminescence from nanocrystals would be last long enough with no need of making new films. However, it was realised that dilute solutions of nanocrystal did not last longer than two weeks. This might be due to the fact that the nanocrystals were contaminated with moisture in the atmosphere. Therefore, a planar mirror with a new film was required for a two-week period.

Due to shortage of planar mirrors, the mirrors needed to be reused which means they had to be washed with solvents. In order to thoroughly clean the cavities, they were sonicated with chloroform. However, this method results in the damage of mirror coating which makes it impossible to obtain a homogenous film on the mirror. These issues were detrimental to the single nanocrystal-cavity experiment.

9.5 Innovation

As mention above, the brand new design of the experimental setup has been innovated in the project by introducing an $x-y$ translation mount to facilitate the tunability of mirrors. Instead of using a fibre-coupled system, the free-beam coupling has been developed which allows less time to align the setup and better mode matching to the cavity mode.

Bibliography

[1] H.-J Briegel, W. Dur, J. I. Cirac, and P. Zoller. *Phys. Rev. Lett.*, 78:3221, 1998.

[2] H. J. Briegel, W. Dur, S. J. van Enk, J. I. Cirac, and P. Zoller. Quantum repeaters. In D. Bouwmeester, A. Ekert, and A. Zeilinger, editors. The Physics of Quantum Information. *Springer, Berlin*, 2000.

[3] A. Kuhn, M. Hennrich, and G. Rempe. Deterministic single-photon source for distributed quantum networking. *Physical Review Letters* 89, 067901, 2002.

[4] B. Lounis and W. E. Moerner. Single photons on demand from a single molecule at room temperature. *Nature* 407, 491, 2000.

[5] A. Gruber et al. Scanning Confocal Optical Microscopy and Magnetic Resonance on Single Defect Centers. *Science* 276, 1997.

[6] B. Lounis, H. Bechtel, D. Gerion, P. Alivisatos, and W. Moerner. Photon antibunching in single CdSe/ZnS quantum dot fluorescence. *Chemical Physics Letters* 329, 399, 2000.

[7] P. Michler et al..Quantum correlation among photons from a single quantum dot at room temperature. *Nature* 406, 968, 2000.

[8] G.Ramon, U. Mizrahi, N. Akopian, S. Braitbart, D. Gershoni, T. L. Reinecke, B. D. Gerardot, P. M. Petroff. Emission characteristics of quantum dots in planar microcavities. *Physical Review B* 73, 205330, 2006.

[9] X. Brokmann, L. Coolen, M. Dahan and J P. Hermier. Measurement of the radiative and non-radiative decay rates of single CdSe nanocrystals through a controlled modification of their spontaneous emission. *Phys. Rev. Lett.* 93 107403, 2004.

[10] X. Brokmann, G. Messin, P. Desbiolles, E. Giacobino, M. Dahan and J P. Hermier. Emission properties of individual CdSe/ZnS quantum dots close to a dielectric interface. *New J. Phys.* 699, 2004.

[11] R. G. Neuhauser, K. T. Shimizu, W. K. Woo, S. A. Empedocles and M. G. Bawendi. Correlation between fluorescence intermittency and spectral diffusion in single semiconductor quantum dots. *Phys. Rev. Lett.* 85 3301, 2000.

[12] G. Schlegel, J. Bohnenberger, I. Potapova and A. Mews. Fluorescence Decay Time of Single Semiconductor Nanocrystals. *Phys. Rev. Lett.* 88 137401, 2002.

[13] O. Labeau, P. Tamarat, and B. Lounis, Temperature dependence of the luminescence lifetime of single CdSe/ZnS quantum dots. *Physical Review Letters* 90, 257404, 2003.

[14] A. Qualtieri, G. Morello, P. Spinicelli, M. T Todaro, T. Stomeo, L. Martiradonna, M. De Giorgi, X. Quelin, S. Buil, A. Bramati, J. P Hermier, R. Cingolani and M. De Vittorio. Nonclassical emission from single colloidal nanocrystals in a microcavity: a route towards room temperature single photon sources. *New J. Phys.,* 11, 2009.

[15] P. R. Dolan, G. M. Hughes, F. Grazioso, B. R. Patton, and J. M. Smith. Femtoliter tunable optical cavity arrays. *Opt. Lett.* 35, 3556 (2010).

[16] Z. Di, H. V. Jones, P. R. Dolan, S. M. Fairclough, J. Fill, G. M. Hughes, and J. M. Smith. Controlling the emission from CdSe/ZnS nanocrystal quantum dots using tunable optical microcavities. *New J. Phys.* 14, 103048, 2012.

[17] K. E. Andersen, C. Y. Fong, W. E. Pickett. Quantum confinement in CdSe nanocrystallites. *Journal of Non-Crystalline Solids,* 299-302 1105-1110, 2002.

[18] C. Kittel, Introduction to Solid State Physics. *John Wiley and Sons Inc.,* 8th edition, 2005.

[19] Al. L. Efros, M. Rosen. Abstract coupling of photophysical and photochemical techniques to microscopy eventually. *Phys. Rev. Lett* 78, 1110, 1997.

[20] P. Moriarty, *Reports on Progress in Physics* 64, 297, 2001.

[21] L. W. Wang, M. Califano, A. Zunger and A. Franceschetti. *Phys. Rev. Lett.* 91 056404, 2003.

[22] V. I. Klimov, A. A. Mikhailovsky, D. W. McBranch, C. A. Leatherdale, M. G. Bawendi, *Science*, 287, 1011-1013, 2000.

[23] V. I. Klimov, J. A. McGuire, R. D. Schaller, V. I. Rupasov, Scaling of multiexciton lifetimes in semiconductor nanocrystals. *Phys. Rev. B,* 77, 195324, 2008.

[24] I. Robel, R. Gresback, U. Kortshagen, R. D. Schaller, V. I. Klimov, Universal size-dependent trend in Auger recombination in direct-gap and indirect-gap semiconductor nanocrystals. *Phys. Rev. Lett.* 102, 177404, 2009.

[25] B. Mahler, P. Spinicelli, S. Buil, X. Quelin, J.P. Hermier, and B. Dubertret, Towards non-blinking colloidal quantum dots, *Nat. Mater.* 7, 659-664, 2008.

[26] X. Wang, X. Ren, K. Kahen, M.A. Hahn, M. Rajeswaran, S. Maccagnano-Zacher, J. Silcox, G.E. Cragg, A.L. Efros, and T.D. Krauss, Non-blinking semiconductor nanocrystals, *Nature* 459, 686-689, 2009.

[27] O. Svelto. Principle of lasers, *Springer New York Dordrecht Heidelberg London*, fifth edition, 2010.

[28] W. L. Erikson and S. Singh. Polarization properties of Maxwell-Gaussian laser beams. *Physical Review E*, Vol 49, 6, 1994.

[29] H. Mabuchi and A. C. Doherty. Cavity quantum electrodynamics: Coherence in context. *Science*, 298 (5591): 1372- 1377, 2002.

[30] E. M. Purcell. Spontaneous emission probabilities at radio frequencies. *Phys. Rev.* 69, 681, 1946.

[31] A. M. Fox. Quantum optics: An Introduction. Chapter 10.3 weak coupling, 201-203, *Oxford University Press*, 2006.

[32] C. T. Yuan, Y. C. Wang, Y. C. Yang, M. C. Wu, Jau Tang, and M. H. Shih. Modification of spontaneous emission rates in single colloidal CdSe/ZnS quantum dots by a submicron-sized dielectric disk. *Applied Physics Letters,* 99(5):053116, 2011.

[33] Y Xu, JS Vuckovic, RK Lee, and OJ Painter. Finite-difference time-domain calculation of spontaneous emission lifetime in a microcavity. *JOSA B*, 16(3), 1999.

[34] B. Lounis and M. Orrit. Single-photon sources. *Rep. Prog. Phys.* 68, 1129, 2005.

[35] A. Beveratos, S. Kuhn, R. Brouri, T. Gacoin, J.-P. Poizat, and P. Grangier. Room temperature stable single-photon source. *Eur. Phys. J. D* 18: 191-196, 2002.

[36] J. M. Gerard, B. Legrand, B. Gayral, E. costard, B. Sermage, R. Kuszelewicz, D. Barrier and V. Thierry. Enhanced Spontaneous Emission by Quantum Boxes in a Monolithic Optical Microcavity. *Phys. Rev. Lett.* 81 1110, 1998.

[37] M.V. Artemyev, U. Woggon, R. Wannemacher, H. Jaschinski, and W. Langbein, Light trapped in a photonic dot: Microspheres act as a cavity for quantum dot emission. *Nano. Lett.* 1, 309-314 (2001).

[38] A. Kiraz, P. Michler, C. Becher, B. Gayral, A. Imamoglu, L. Zhang, and E. Hu. Cavity-quantum electrodynamics using a single InAs quantum dot in a microdisk structure. *Appl. Phys. Lett.* 78, 3932, 2001.

[39] K. J. Vahala. Optical microcavities. *Nature*, 424(695): 839-846, 2003.

[40] E. Moreau, I. Robert, J. M. Gerard, I. Abram, L. Manin, V. Thierry-Mieg. Single-mode solid-state single photon source based on isolated quantum dots in pillar microcavities. *Appl. Phys. Lett.* 79, 2865, 2001.

[41] G. S. Solomon, M. Pelton, Y. Yamamoto. Single-mode Spontaneous Emission from a Single Quantum Dot in a Three-Dimensional Microcavity. *Phys. Rev. Lett.* 86, 3903, 2001.

[42] O. G. Schmidt Ed., Lateral Alignment of Epitaxial Quantum Dots. *Berlin, Germany: Springer*, 2007.

[43] C. Schneider, T. Heindel, A. Huggenberger, P. Weinmann, C. Kistner, M. Kamp, S. Reizenstein, S. Hofling, and A. Forchel. Single photon emission from a site-controlled quantum dot-micropillar cavity system. *Appl. Phys. Lett.* 94:1111111-1111113, 2009.

[44] F. Albert, S. Stobbe, C. Schneider, T. Heindel, S. Reitzenstein, S. Hofling, P. Lodahl, L. Worschech and A. Forchel, Quantum efficiency and oscillator strength of site-controlled InAs quantum dots. *Appl. Phys. Lett., Vol* 96:1511021-1511023, 2010.

[45] A. Dousse, L. Lanco, J. Suffczynski, E.Semenova, A. Miard, A. Lemaitre, I. Sagnes, C. Roblin, J. Bloch, and P. Senellart, Controlled light-matter coupling for a single quantum dot embedded in a pillar microcavity using far-field optical lithography. *Phys. Rev. Lett. Vol.* 101: 2674041-2674044, 2008.

[46] C. Kistner, K. Morgener, S. Reitzenstein, C. Schneider, S. Hofling, L. Worschech, A. Forchel, P. Yao, and S. Hughes. Strong coupling in a quantum dot micropillar system under electrical current injection. *Appl. Phys. Lett., vol.* 96: 2211021-2211023, 2010.

[47] H. Y. Ryu and M. Notomi, Enhancement of spontaneous emission from the resonant modes of a photonic crystal slab singe-defect cavity. *Opt. Lett.* 28, 2390 (2003).

[48] A. Qualtieri, G. Morello, P. Spinicelli, M. T. Todaro, T. Stomeo, L. Martiradonna, M. De Giorgi, S. Buil, X. Qulin, A. Bramati, J. P. Hermier, R. Cingolani, and M. De Vittorio. Room temperature single-photon sources based on single colloidal nanocrystals in microcavities. *Superlattices and Microstructures* 47:187-191, 2010.

[49] O. Fedorych, C. Kruse, A. Ruban, D. Hommel, G. Bacher *et al.* Room temperature single photon emission from an epitaxially grown quantum dot. *Appl. Phys. Lett.* 100, 061114, 2012.

[50] W.-Y. Chen, W.-H. Chang, H.-S. Chang, T.M. Hsu, Chien-Chieh Lee et al. Enhanced light emission from InAs quantum dots in single-defect photonic crystal microcavities at room temperature. *Appl. Phys. Lett.* 87, 071111, 2005.

[51] Z. Wu, Z. Mi, P. Bhattacharya. T. Zhu, and J. Xu. Enhanced spontaneous emission at 1.55 Îijm from colloidal PbSe quantum dots in a Si photonic crystal microcavity. *Appl. Phys. Lett.* 90, 171105, 2007

[52] J. Renner, L. Worschech, A. Forchel, S. Mahapatra, and K. Brunner. Whispering gallery modes in high quality ZnSe/ZnMgSSe microdisks with CdSe quantum dots studied at room temperature. *Appl. Phys. Lett.* 89, 091105, 2006.

[53] A. Pitanti, M. Ghulinyan, D. Navarro-Urrios, G. Pucker, and L.Pavesi. Probing the Spontaneous Emission Dynamics in Si-Nanocrystals-Based Microdisk Resonators. *Phys. Rev. Lett.* 104, 103901, 2010.

[54] T. Baba, D. Sano, K. Nozaki, K. Inoshita, Y. Kuroki, and F. Koyama. Observation of fast spontaneous emission decay in GaInAsP photonic crystal point defect nanocavity at room temperature. *Applied Physics Letters, vol.* 85, no. 18, pp. 3989âĂŞ3991, 2004.

[55] J. M. Gerard, J. B. Genin, J. Lefebvre, J. M. Mosison, N. Lebouche, F. Barthe: Semiconductor Microcavities, Quantum Boxes and the Purcell Effect. *J. Crystal Growth* 150, 351, 1995.

[56] B. Gayral, J. M. Gerard, B. Sermage, A. Lemaitre, and C. Dupuis. Time-resolved probing of the Purcell effect for InAs quantum boxes in GaAs microdisks. *Appl. Phys. Lett.* 78, 2828, 2001. DOI: 10.1063/1.1370123.

[57] G. Ramon, U. Mizrahi, N. Akopian, S. Braitbart, D. Gershoni, T. L. Reinecke, B. D. Gerardot, and P. M. Petroff. Emission characteristics of quantum dots in planar microcavities. *Phys. Rev. B* 73, 205330, 2006.

[58] G. V. Prakash, L. Besombes, T. Kelf, J. J. Baumberg. Tunable resonant optical microcavities by self-assembled templating. *Optics Lett. Vol.* 29, No 13, 2004.

[59] G. Cui, J. M. Hannigan, R. Loeckenhoff, F. M. Matinaga, M. G. Raymer, S. Bhongale, M. Holland, S. Mosor, S. Chatterjee, H. M. Gibbs, and G. Khitrova. A hemispherical, high solid angle optical microcavity for cavity-QED studies. *Opt Express,* 14(6):2280-2299, 2006.

[60] A. Muller, E. B. Flagg, M. Metcalfe, J. Lawall, and G. S. Solomon. Coupling an epitaxial quantum dot to a fiber-based external-mirror microcavity. *Applied Physics Letters*, 95(3): 173101-173103, 2009.

[61] D. Hunger, T. Steinmetz, Y. Colombe, C. Deutsch, T. W. Hansch, and J. Reichel. A fiber FabryPerot cavity with high finesse. *New Journal of Physics,* 12(6):065038, 2010.

[62] A. Muller, E. B. Flagg, J. R. Lawall, and G. S. Solomon. Ultrahigh-finesse, low-mode-volume FabryPerot microcavity. *Optics Letters,* 35 (13): 2293-2295, 2010.

[63] R. J. Barbour, P. A. Dalgarno, A. Curran, K. M. Nowak, H. J. Baker, D. R. Hall, N. G. Stoltz, P. M. Petroff, and R. J. Warburton. A tunable microcavity. *Applied Physics Letters*, 110(5): 053107-05311, 2011.

[64] D. Hunger, C. Deutsch, R. J. Barbour, R. J. Warburton, and J. Reichel. Laser microfabrication of concave, low roughness features in silica. *AIP ADVANCES* 2, 012119, 2012.

[65] S. Buckley, K. Rivoire, J. Vuckovic. Engineered Quantum dot Single Photon Sources. *Reports on Progress in Physics*, 75, 1126503, 2012.

[66] M. Xiao, L. Wu and H. J. Kimble. Detection of amplitude modulation with squeezed light for sensitivity beyond the shot-noise limit. *Physical Review Letters* 59, 278, 1987.

[67] M. A. Nielsen and I. L. Chuang. Quantum Computation and Quantum Information, *Cambridge University Press*, 2000.

[68] M. Benyoucef, P. Michler and S. M. Ulrich. Semiconductor single-photon sources, *Themenheft Forschung Photonic.* WWW. uni-stuttgart. de/hkom/publikationen/themenheft/ 02/semiconductor. pdf.